International Journal of Mechanical Sciences 329 (2026) 112080



Contents lists available at ScienceDirect

International Journal of Mechanical Sciences

journal homepage: www.elsevier.com/locate/ijmecsci





# Hybrid data-physics-informed neural network framework for reconstruction-driven Helmholtz resonator design

Hangxing Li, Yang Song, Li Cheng *

*Department of Mechanical Engineering, The Hong Kong Polytechnic University, Hong Kong SAR, China*

ARTICLE INFO

*Keywords:*
Sound field reconstruction
Physics-informed neural networks
Passive noise control
Sensor placement optimization
Helmholtz resonator
Sparse measurement

ABSTRACT

Effective noise suppression in acoustic enclosures often relies on precisely tuned Helmholtz resonators (HRs). However, conventional design methodologies are hindered by the unavailability of accurate analytical models, especially for complex-shaped cavities, and the practical infeasibility of dense three-dimensional acoustic field measurements. To overcome these limitations, this paper proposes a hybrid Data-Physics-Informed Neural Network (Data-PINN) framework for reconstruction-driven HR design using sparse microphone measurements. First, a spatial-frequency decomposition strategy decouples the acoustic response: environmentally sensitive frequency-dependent characteristics are directly extracted from sparse microphone measurements, while the relatively stable spatial pressure distributions are reconstructed via a PINN constrained by a homogeneous Helmholtz equation. Second, a bi-level discrete optimization framework hierarchically determines optimal sensor placements within physically realizable discrete grids, maximizing both signal-to-noise ratio and spatial observability. Finally, leveraging the reconstructed full-field pressure, an analytical design methodology based on Excitation-Dependent Representative Basis (EDRB) decomposition and fixed-point theory is proposed to determine the optimal HR parameters. Numerical and experimental validations on both a canonical rectangular cavity and a complex helicopter cabin mockup demonstrate the high fidelity of the proposed framework in reconstructing the acoustic field, achieving a normalized mean squared error of less than $7 \times 10^{-3}$. Consequently, this enables HR designs that achieve noise suppression performance within a 3 dB deviation from the ground-truth benchmark. (Code available at GitHub: https://github.com/HengistLi/Hybrid-Data-PINN-Framework-for-Reconstruction-Driven-HR-Design)

## 1. Introduction

Effective noise suppression is critical for acoustic comfort and public health [1–7], with Helmholtz resonator (HR) serving as one of the effective passive control devices. However, the complexity of engineering systems often precludes accurate analytical modelling, rendering data-driven design a compelling alternative [8,9]. Constrained by the impracticality of dense sensor deployment, sound field reconstruction has emerged as a pivotal technique, enabling high-fidelity pressure field estimation from sparse measurements and paving the way for reconstruction-driven noise control.

Although HRs [10–15] are effective for noise control of acoustic enclosures owing to their resonant characteristics, their performance critically depends on precise parameter tuning. While optimal HR design is tractable when accurate analytical acoustic models are available [16], such models are often unattainable for complex-shaped enclosures. To circumvent comparable limitations in vibration control, a data-driven design methodology for mechanical absorbers leveraging dense displacement field data was recently proposed [17–19]. However, extending this paradigm to acoustic domains presents distinct challenges: (i) acoustic sensors are typically intrusive [20–22], in contrast to the non-contact laser vibrometers employed in vibration testing [23–26]; and (ii) whereas vibration analysis typically focuses on two-dimensional surface responses of vibrating structures, acoustic characterization necessitates three-dimensional pressure field measurements. The practical infeasibility of conducting dense three-dimensional pressure scans on complex geometries therefore underscores the necessity of a reconstruction-driven design framework founded on sparse measurements.

Contemporary sound field reconstruction [27–31] methodologies can be broadly categorized into four paradigms.

* Corresponding author.
*E-mail address:* li.cheng@polyu.edu.hk (L. Cheng).

https://doi.org/10.1016/j.ijmecsci.2026.112080
Received 7 June 2026; Received in revised form 2 September 2026; Accepted 2 September 2026
Available online 3 September 2026
0020-7403/© 2026 Elsevier Ltd. All rights are reserved, including those for text and data mining, AI training, and similar technologies.

(i) Analytical solution-driven methods: these approaches employ basis function expansions [32–35] derived from analytical solutions of the governing acoustic wave equation. However, for geometries with irregular or complex boundaries, accurately resolving expansion coefficients necessitates dense measurement data [36,37], limiting their applicability in practical engineering scenarios.

(ii) Sparse prior-driven methods: to mitigate sensor deployment constraints, techniques leveraging compressive sensing and sparse regularization have been developed [38,39]. Nevertheless, their performance remains highly sensitive to measurement noise and critically dependent on predefined sparsity assumptions, which undermines their robustness in complex acoustic environments.

(iii) Data-driven methods: capitalizing on advances in deep learning [40–48], supervised neural networks have been employed to learn implicit mappings between sparse observations and full-field pressure distributions [49,50]. However, their efficacy is contingent upon large-scale labeled datasets, a prerequisite that fundamentally conflicts with the severe data scarcity inherent to three-dimensional acoustic field measurement.

(iv) Physics-driven methods: to circumvent reliance on labeled data, Physics-Informed Neural Networks (PINNs) [51–56] embed governing physical laws directly into the loss function as residual constraints. This paradigm enables interpretable solutions for complex problems across diverse disciplines. In fluid mechanics, PINNs are extensively employed for forward and inverse analyses [57,58], flow field reconstruction from sparse observations [59–61], and the modelling of fluid-structure interaction problems [62,63]. In materials science, they find applications such as identification of electrochemical parameters [64,65], monitoring of battery health [66–69] etc. Furthermore, in solid mechanics [70], PINNs have been successfully applied to characterize viscoelastic properties [71] and predict crack propagation in solids [72]. While this unsupervised paradigm theoretically enables reconstruction from sparse measurements, conventional implementations typically presuppose complete knowledge of the inhomogeneous Helmholtz equation [73]. In practical engineering scenarios, however, the acoustic excitation term is difficult to characterize accurately and remains highly sensitive to environmental fluctuations [74–84]. Furthermore, standard PINNs encounter severe optimization bottlenecks when extended to high-dimensional, frequency-dependent three-dimensional acoustic fields [85,86]. Meanwhile, the joint minimization of competing loss components inherently induces gradient conflicts [87–89]. Furthermore, the prohibitively large parameter space exacerbates convergence instability. Ultimately, these factors compromise training stability and reconstruction fidelity.

In addition to the reconstruction algorithm itself, the fidelity of sound field reconstruction is fundamentally governed by the spatial configuration of sensors [90–100]. Inadequate or suboptimal sensor coverage inherently limits observational data, rendering high-fidelity field estimation a formidable challenge. While optimizing microphone placement could theoretically alleviate this limitation, direct gradient-based optimization is impeded by the non-differentiable nature of discrete mounting locations. Continuous relaxation strategies, such as differentiable search methods leveraging bilinear interpolation [101], have been proposed to enable concurrent optimization of sensor coordinates and network parameters. However, the pronounced dimensionality disparity between the high-dimensional neural weights and low-dimensional sensor coordinates frequently induces training instabilities. Although bi-level optimization architectures [102] have been introduced to hierarchically decouple these tasks, existing implementations predominantly operate within continuous spatial domains. Consequently, they fail to enforce strict adherence to discrete, physically realizable mounting locations, limiting their practical engineering applications.

To address these interconnected challenges, a reconstruction-driven framework for passive noise control inside acoustic enclosures is proposed, which integrates a hybrid data-PINN architecture with discrete sensor optimization. This methodology is built upon three key innovations:

(i) **Hybrid Data-PINN Field Reconstruction**. To circumvent the prohibitive parameter space and source-term identification challenges inherent to three-dimensional frequency-dependent PINNs, a spatial-frequency decomposition strategy is introduced. Frequency-dependent components are extracted directly from sparse acoustic measurements, while spatial distributions are reconstructed from sparse to dense fields via a PINN. This decoupling strategy drastically reduces trainable parameters and transforms the governing inhomogeneous Helmholtz equation into a homogeneous form, thereby eliminating the need for explicit source characterization. Furthermore, a conflict-free gradient alignment strategy is integrated to harmonize competing PDE and data loss gradients, ensuring stable convergence.

(ii) **Bi-level Discrete Optimization Framework**. Recognizing that practical sensor deployment is constrained to discrete mounting points, a bi-level discrete optimization architecture is developed. This framework hierarchically decouples high-dimensional network training from low-dimensional sensor positioning, ensuring optimized sensor spatial configurations remain strictly within a discretized search space while maximizing the signal-to-noise ratio for frequency identification and satisfying observability requirements for spatial reconstruction.

(iii) **Reconstruction-driven HR Design**. To bridge the acoustic field reconstruction and passive noise control, an analytical design methodology is established. Leveraging the reconstructed pressure field, the framework employs Excitation-Dependent Representative Basis (EDRB) decomposition and fixed-point theory to analytically determine the optimal HR parameters, enabling direct design of acoustic absorbers from sparse sensor data.

It is worth noting that the proposed hybrid Data-PINN framework can be embedded into other acoustic control strategies, wherever the knowledge of accurate spatial pressure distribution is needed. This study uses the EDRB-based HR analytical design as an example to establish a complete, closed-loop reconstruction-driven engineering workflow.

The remainder of this paper is organized as follows. Section 2 details the theoretical framework, encompassing the hybrid data-PINN reconstruction architecture and the reconstruction-driven design methodology for Helmholtz resonators. Section 3 validates the proposed framework through numerical simulations on a rectangular acoustic cavity. Section 4 presents experimental validations, first on a rectangular cavity to demonstrate design accuracy, and subsequently on a helicopter cabin to verify the method's robustness and applicability to complex, arbitrarily shaped geometries. Conclusions are summarized in Section 5.

## 2. Theoretical framework

This section establishes the theoretical foundation of the proposed reconstruction-driven design method. The framework operates through a sequential two-stage pipeline: (i) a hybrid Data-PINN architecture that reconstructs high-fidelity, full-field acoustic pressure from sparse microphone measurements, and (ii) an analytical design methodology that leverages the reconstructed field to determine the optimal HR parameters for noise suppression.

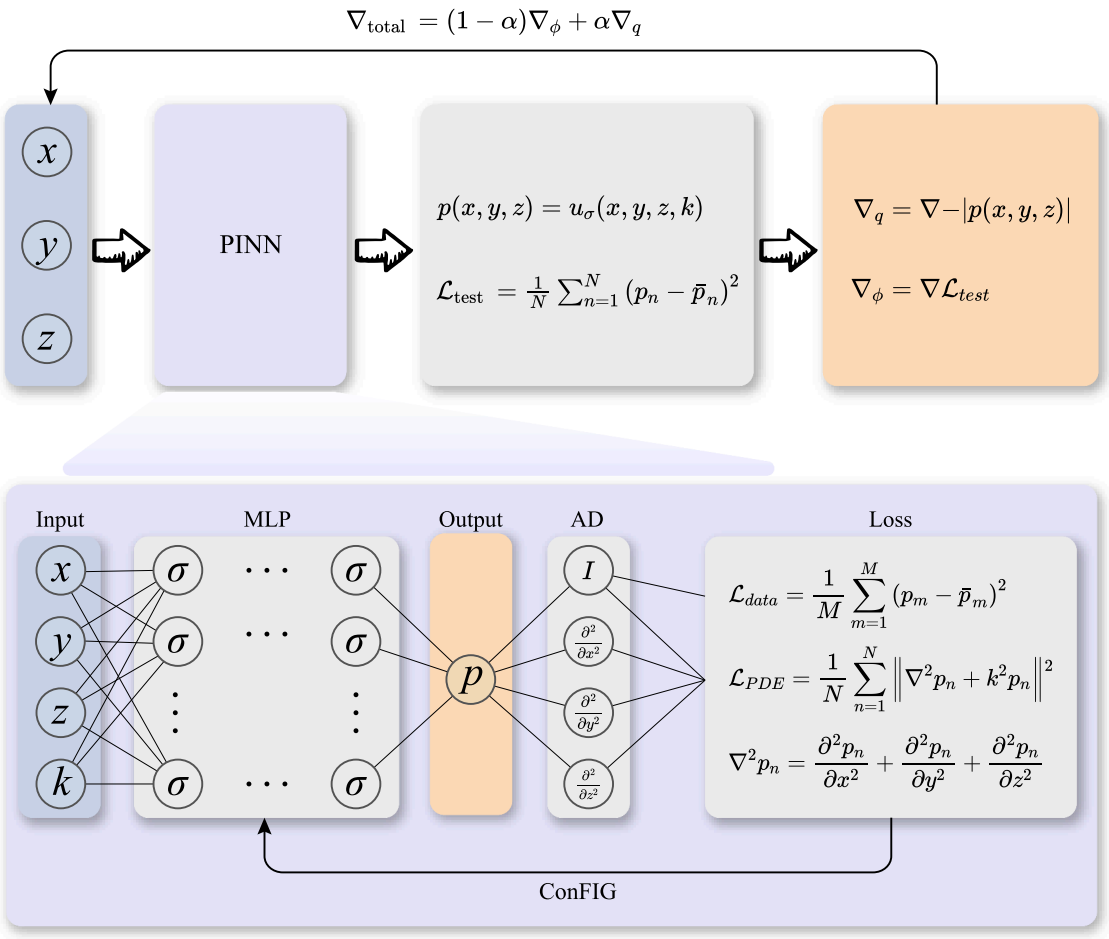



**Fig. 1.** Schematic illustration of the hybrid data-PINN reconstruction framework. The framework employs a bi-level optimization strategy: (i) an inner loop in which the PINN is trained on Helmholtz equation and sparse measurements using the ConFIG method for stable convergence, utilizing a dataset of $N$ spatial points and $I$ wavenumbers to form $N \times I$ combined training samples; and (ii) an outer loop that determines optimal sensor locations to capture frequency-dependent components and facilitate high-fidelity spatial reconstruction.

### 2.1. Hybrid data-PINN network architecture

The acoustic field within an arbitrarily shaped enclosure is governed by the inhomogeneous Helmholtz equation [103]:

$$\nabla^2 p(\mathbf{r},s) + k^2 p(\mathbf{r},s) = f(\mathbf{r},s), \tag{1}$$

where $\nabla^2$ denotes the Laplace operator; $k$ the wavenumber; $\mathbf{r}$ the spatial coordinate; $s$ the complex variable; $p(\mathbf{r},s)$ the acoustic pressure field; and $f(\mathbf{r},s)$ the sound source distribution. Direct application of conventional PINNs to Eq. (1) in practical engineering scenarios faces three critical bottlenecks: (i) the source term $f(\mathbf{r},s)$ is difficult to characterize accurately; (ii) the frequency response is highly susceptible to environmental fluctuations and operational variations; and (iii) extending PINNs to three-dimensional, frequency-dependent fields drastically inflates the trainable parameter space, exacerbating optimization instability.

To circumvent these limitations, a spatial-frequency decomposition strategy is introduced based on the method of separation of variables. The acoustic pressure field is decomposed into frequency-dependent and spatial components via separation of variables, effectively decoupling the environmentally susceptible operational variations from the relatively stable spatial pressure distributions [104]:

$$p(\mathbf{r},s) = \sum_{i=1}^{I} \phi_i(\mathbf{r}) q_i(s), \tag{2}$$

where $q_i(s)$ captures the frequency-dependent characteristics (e.g., source strength and environmental fluctuations), and $\phi_i(\mathbf{r})$ represents the spatial functions characterizing the global energy distribution. The environmentally sensitive frequency-dependent components are directly identified in real-time from sparse microphone measurements, whereas the relatively stable spatial pressure distributions are reconstructed via a PINN. Notably, this decoupling strategy reformulates the governing inhomogeneous Helmholtz equation into a homogeneous form constrained solely by spatial coordinates, effectively circumventing the need for explicit source term characterization and drastically reducing the neural network's trainable parameter space.

Accurately extracting $q_i(s)$ and reconstructing $\phi_i(\mathbf{r})$ require a strategically optimized sensor layout. This layout must simultaneously maximize the signal-to-noise ratio for frequency identification and ensure sufficient spatial observability for the PINN. This requirement is formalized as a multi-objective optimization problem:

$$\nabla_{\text{total}} = (1-\alpha)\nabla_\phi + \alpha\nabla_q, \tag{3}$$

where $\nabla_q$ denotes the gradient of the identification loss for the frequency-dependent components with respect to the sensor coordinates. Empirically, positioning sensors at locations exhibiting maximum acoustic pressure amplitude would enhance the signal-to-noise ratio, thereby improving the extraction accuracy of these components. Consequently, this gradient term can be approximated by the spatial distribution gradient, expressed as $\nabla_q = \nabla(-|\phi(\mathbf{r})|)$. Similarly, $\nabla_\phi$ represents the gradient of the PINN reconstruction loss with respect to sensor locations, where $\alpha$ serves as a weighting hyperparameter.

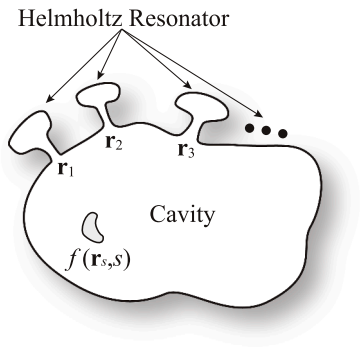



**Fig. 2.** Schematic of an arbitrarily shaped acoustic cavity coupled to multiple HRs. The primary cavity is excited by a sound source located at $\mathbf{r}_s$, and the $n$-th HR is positioned at $\mathbf{r}_n$.

Given that the PINN focuses exclusively on reconstructing the spatial components, the Helmholtz equation is imposed as a physical constraint, formulated as:

$$\sum_{i=1}^{I}\left(\nabla^2\phi_i(\mathbf{r})+k_i^2\phi_i(\mathbf{r})\right)=0. \tag{4}$$

Consequently, the PDE residual loss function for the PINN is defined as:

$$\mathscr{L}_{\text{PDE}}=\frac{1}{N}\sum_{i=1}^{I}\sum_{n=1}^{N}\left(\nabla^2\phi_i(\mathbf{r}_n)+k_i^2\phi_i(\mathbf{r}_n)\right)^2, \tag{5}$$

where $N$ denotes the total number of sample points for reconstruction, and $\phi_i(\mathbf{r}_n)$ the PINN-predicted value of the $i$-th spatial function at the $n$-th spatial location. However, relying solely on the PDE loss term is insufficient to ensure solution uniqueness. Consequently, a supervised data loss function is incorporated to align the network predictions with observed measurements, defined as:

$$\mathscr{L}_{\text{data}}=\frac{1}{M}\sum_{i=1}^{I}\sum_{m=1}^{M}\left(\phi_i(\mathbf{r}_m)-\overline{\phi}_i(\mathbf{r}_m)\right)^2, \tag{6}$$

where $M$ denotes the total number of sparse measurement points; $\phi_i(\mathbf{r}_m)$ the PINN-predicted value of the $i$-th spatial function at the $m$-th spatial location; and $\overline{\phi}_i(\mathbf{r}_m)$ the corresponding measured acoustic pressure.

During backpropagation, the competing objectives of $\mathscr{L}_{\text{PDE}}$ and $\mathscr{L}_{\text{data}}$ frequently generate conflicting gradient directions, leading to optimization stagnation. To resolve this, the Conflict-Free Inverse Gradients (ConFIG) method [105] is employed. ConFIG constructs an update direction that maintains a strictly positive projection onto each individual loss gradient, thereby mitigating interference without requiring manual hyperparameter tuning. The resulting conflict-free gradient is formulated as:

$$\mathscr{G}(\mathbf{g}_{\text{data}},\mathbf{g}_{\text{PDE}})=\left(\mathbf{g}_{\text{data}}^T\mathbf{g}_v+\mathbf{g}_{\text{PDE}}^T\mathbf{g}_v\right)\mathbf{g}_v, \tag{7}$$

where $\mathbf{g}_{\text{data}}$ and $\mathbf{g}_{\text{PDE}}$ denote the gradients of the data-fidelity and PDE-residual loss functions with respect to the trainable network parameters, and $\mathbf{g}_v$ is given by:

$$\mathbf{g}_v=\mathscr{U}[\mathscr{U}(\mathscr{O}(\mathbf{g}_{\text{data}},\mathbf{g}_{\text{PDE}}))+\mathscr{U}(\mathscr{O}(\mathbf{g}_{\text{PDE}},\mathbf{g}_{\text{data}}))], \tag{8}$$

where $\mathscr{U}(\mathbf{g}_i)=\mathbf{g}_i/|\mathbf{g}_i|$ denotes the normalization operator, while the orthogonality operator is defined as:

$$\mathscr{O}(\mathbf{g}_{\text{data}},\mathbf{g}_{\text{PDE}})=\mathbf{g}_{\text{PDE}}-\frac{\mathbf{g}_{\text{data}}^T\mathbf{g}_{\text{PDE}}}{|\mathbf{g}_{\text{data}}|^2}\mathbf{g}_{\text{data}}. \tag{9}$$

To ensure stable convergence, the optimization problem formulated in Eq. (3) is resolved through a hierarchical bi-level strategy, as schematically illustrated in Fig. 1. This architecture decouples the high-dimensional neural network training from the low-dimensional spatial search, thereby circumventing the optimization instabilities typically induced by concurrent updates across vastly different parameter scales. Specifically, the inner loop fixes the sensor coordinates and iteratively updates the PINN parameters to minimize the reconstruction loss. Upon convergence, the outer loop leverages the stabilized loss landscape and model output $u_\sigma(x,y,z,k)$ to update sensor positions, systematically probing configurations that maximize both frequency-domain observability and spatial reconstruction fidelity.

Crucially, this spatial optimization is strictly enforced within a discrete mounting grid rather than a continuous domain. In practical engineering scenarios, microphone deployment is typically constrained by structural boundaries, pre-drilled mounting arrays, or standardized sensor brackets. Conventional continuous relaxation methods frequently yield fractional coordinates that necessitate post-hoc rounding or interpolation, which may degrade reconstruction accuracy and violates physical hardware limits. By restricting the search to a discretized space, the proposed bi-level framework guarantees that the optimized layout is directly manufacturable and experimentally implementable without geometric approximation. This discrete-constrained paradigm bridges the gap between algorithmic optimality and real-world engineering feasibility, providing a robust foundation for the subsequent reconstruction-driven HR design detailed in Section 2.2.

In summary, the proposed reconstruction framework proceeds as follows:

(i) **Sparse Measurement and Decomposition**: Measure the acoustic pressure responses $p(\mathbf{r}_m,s)$ at $M$ sparse microphone locations, and perform Singular Value Decomposition (SVD) on the measured pressure matrix to extract the spatial functions $\phi_i(\mathbf{r}_m)$ and the frequency-dependent components $q_i(s)$.

(ii) **Bi-level Optimization**: Reconstruct the spatial components $\phi_i(\mathbf{r}_n)$ over a dense domain from sparse observations $\phi_i(\mathbf{r}_m)$, and simultaneously update the frequency-dependent components $q_i(s)$ via the proposed bi-level optimization strategy (Fig. 1).

(iii) **Full-field Synthesis:** Synthesize the full-field pressure response $p(\mathbf{r}_n,s)$ by superimposing the reconstructed spatial functions $\phi_i(\mathbf{r}_n)$ and the updated frequency-dependent components $q_i(s)$ via Eq. (2).

The critical assumption is that, with strategically placed sensors, the frequency-dependent components $q_i(s)$ extracted from sparse measurements are representative of those that would be obtained from dense measurements. This assumption is physically justified for linear acoustic systems, as all spatial points within the enclosure share the same resonant characteristics. Consequently, the dominant dynamic features are captured even when the sampling is sparse, provided the sensors are strategically placed at acoustically relevant locations. However, this assumption holds most rigorously for low-order spatial functions. High-order spatial functions, which exhibit complex spatial fluctuations and shorter wavelengths, require a denser measurement array to ensure reconstruction fidelity.

### 2.2. Reconstruction-driven analytical design for Helmholtz resonators

With the full-field pressure $p(\mathbf{r},s)$ reconstructed, the framework proceeds to analytically determine the optimal HR parameters (volume, resonant frequency and damping ratio). Consider an arbitrarily shaped acoustic cavity coupled to multiple HRs positioned at $\mathbf{r}_n$, excited by a source at $\mathbf{r}_s$, as illustrated in Fig. 2.

Motion equation of this coupled system can be formulated as

$$\nabla^2p(\mathbf{r},s)-\frac{s^2}{c_0^2}p(\mathbf{r},s)+s\rho_0\sum_{n=1}^{N}q_n(s)\delta(\mathbf{r}-\mathbf{r}_n)\&=sf(s)\delta(\mathbf{r}-\mathbf{r}_s), \tag{10.a}$$

**Table 1**
Architecture and hyperparameters of the PINN model.

| Parameter | Configuration | Parameter | Configuration |
|---|---|---|---|
| Input variables | 4 $(x,y,z,k)$ | Hidden layers | 4 layers × 64 neurons |
| Activation function | Tanh | Weight initialization | Xavier normal |
| Output variable | 1 $(p)$ | Optimizer | Adam |
| Learning rate | $1 \times 10^{-4}$ | Batch size | Full-batch |
| Epochs | 10,000 | Random seed | 19,018 |
| Collocation points | 4096 | Sampling method | Uniform grid |

$$\left(s^2 m_n + s c_n + k_n\right) y_n(s) \& = -p(\mathbf{r}_n, s) S_n, \tag{10.b}$$

where $c_0$ and $\rho_0$ are the speed of sound and ambient air density, respectively; $q_n(s)$ and $f(s)$ the volume velocity source strengths per unit volume for the $n$-th HR and source; $\delta(\cdot)$ the Dirac delta function; $\mathbf{r}_n$ and $\mathbf{r}_s$ their respective position vectors; and $m_n$, $c_n$, $k_n$, $y_n(s)$ and $S_n$ the HR mass, damping, stiffness, displacement and cross-sectional area in the lumped parameter model.

The volume velocity of the $n$-th HR is given by

$$q_n(s) = s S_n y_n(s). \tag{11}$$

Substituting Eqs. (11) and (10.b) into Eq. (10.a) yields

$$-\nabla^2 p(\mathbf{r}, s) + \frac{s^2}{c_0^2} p(\mathbf{r}, s) + s^2 \rho_0 \sum_{n=1}^{N} S_n^2 \frac{p(\mathbf{r}, s)\delta(\mathbf{r} - \mathbf{r}_n)}{s^2 m_n + s c_n + k_n} = -s f(s) \delta(\mathbf{r} - \mathbf{r}_s). \tag{12}$$

Given that the acoustic pressure $p(\mathbf{r}, s)$ is reconstructed via the framework established in Section 2.1, the sound field can be decomposed using the Excitation-Dependent Representative Basis (EDRB) [17, 18], formulated as:

$$p(\mathbf{r}, s) = \mathbf{U}\Sigma\mathbf{V}^{\mathrm{H}}, \tag{13}$$

where $(\cdot)^{\mathrm{H}}$ denotes conjugate transpose; $\mathbf{U}$ and $\mathbf{V}$ the matrices of left and right singular vectors. The diagonal matrix $\mathbf{\Sigma}$ contains the non-negative singular values. The truncation order is determined using a cumulative energy criterion, retaining the minimum number of dominant singular vectors required to capture 90% of the total sum of singular values.

Substituting Eq. (13) into Eq. (12) yields

$$\left( -\nabla^2 \mathbf{U} + \frac{s^2}{c_0^2} \mathbf{U} \right) \mathbf{\Sigma} \mathbf{V}^{\mathrm{H}} + s^2 \rho_0 \sum_{n=1}^{N} S_n^2 \frac{\mathbf{U}\delta(\mathbf{r} - \mathbf{r}_n)}{s^2 m_n + s c_n + k_n} \mathbf{\Sigma} \mathbf{V}^{\mathrm{H}} = -s f(s) \delta(\mathbf{r} - \mathbf{r}_s). \tag{14}$$

Using Helmholtz equation gives

$$\nabla^2 \mathbf{U} + \frac{\boldsymbol{\Omega}^2}{c_0^2} \mathbf{U} = 0, \tag{15}$$

where $\boldsymbol{\Omega}$ represents resonant frequencies of EDRBs. Eq. (14) can then be rewritten as

$$\left(s^2 \mathbf{E} + \boldsymbol{\Omega}^2\right) \mathbf{U}\Sigma\mathbf{V}^{\mathrm{H}} + s^2 \rho_0 c_0^2 \sum_{n=1}^{N} S_n^2 \frac{\mathbf{U}\delta(\mathbf{r} - \mathbf{r}_n)}{s^2 m_n + s c_n + k_n} \mathbf{\Sigma} \mathbf{V}^{\mathrm{H}} = -s c_0^2 f(s) \delta(\mathbf{r} - \mathbf{r}_s). \tag{16}$$

Multiplying both sides of this equation by $\mathbf{U}^{\mathrm{T}}$ and integrating over the cavity volume yield

$$\left[ \left(s^2 \mathbf{E} + \boldsymbol{\Omega}^2\right) \boldsymbol{\Lambda} + \sum_{n=1}^{N} h_n \boldsymbol{\theta}_n \boldsymbol{\theta}_n^{\mathrm{T}} \right] \mathbf{X} = \mathbf{F}, \tag{17}$$

where

$$\boldsymbol{\Lambda} = \int_V \mathbf{U}^{\mathrm{T}} \mathbf{U} dV, \ \mathbf{X} = \mathbf{\Sigma}\mathbf{V}^{\mathrm{H}}, \ \mathbf{F} = -s c_0^2 f(s) \int_V \mathbf{U}^{\mathrm{T}} \delta(\mathbf{r} - \mathbf{r}_s) dV$$
$$\boldsymbol{\theta}_n = \int_V \mathbf{U}^{\mathrm{T}} \delta(\mathbf{r} - \mathbf{r}_n) dV, h_n = \frac{s^2 \omega_n^2 V_n}{s^2 + 2 s \omega_n \xi_n + \omega_n^2} \quad , \tag{18}$$
$$\xi_n = \frac{c_n}{2 m_n \omega_n}, \ \omega_n = \sqrt{\frac{k_n}{m_n}}, k_n = \frac{\rho_0 c_0^2 S_n^2}{V_n}$$

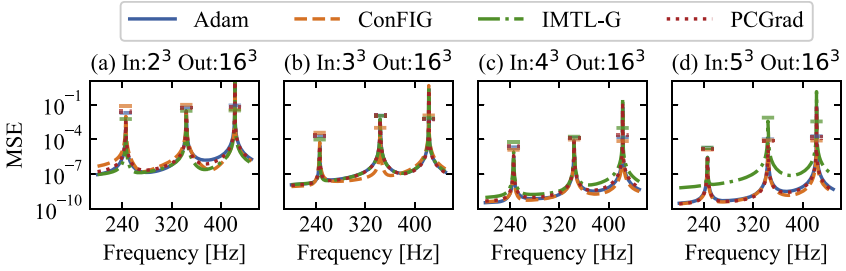



**Fig. 3.** MSE of sound field reconstruction versus the number of sparse microphones for different optimization algorithms. Horizontal line segments in each subfigure indicate the MSE of the three dominant spatial components reconstructed by the PINN. The full-field acoustic pressure, reconstructed by combining these spatial components with measured frequency-dependent components via Eq. (2), is shown as curves representing the overall reconstruction MSE.

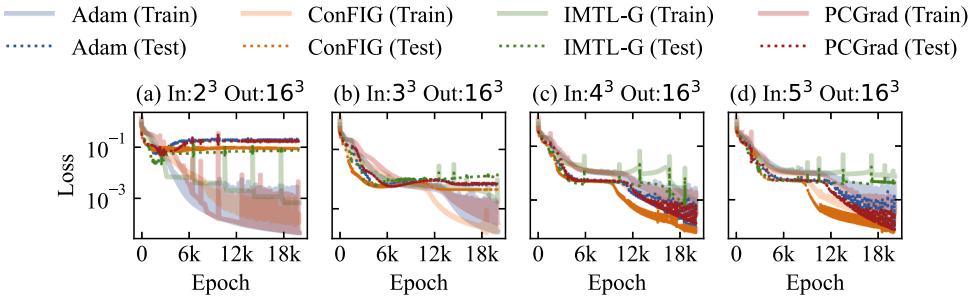



**Fig. 4.** Training and testing losses versus the number of sparse microphones for different optimization algorithms. The divergence between the training and testing losses at low microphone counts (e.g., 8) indicates overfitting, whereas the convergence of both losses at higher counts (e.g., 27) demonstrates stable reliability. ConFIG consistently yields the lowest testing loss and stable convergence profile.

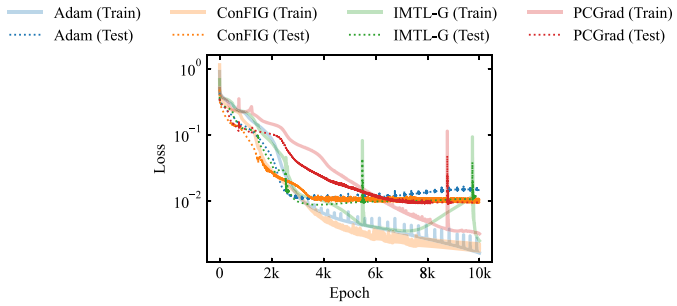



**Fig. 5.** Training and testing losses for the 20-microphone configuration across different optimization algorithms. Consistent with the analysis in Fig. 4, the ConFIG method exhibits the lowest and most stable testing loss, confirming its superiority in resolving gradient conflicts during PINN training.

in which $V_n$ denotes the volume of the $n$-th HR.

According to Eq. (17), the transfer function of the $i$-th EDRB can be expressed as

$$H_i = \frac{X_i}{F_i} = \frac{1}{\left(s^2 + \Omega_i^2\right)\Lambda_i + \sum_{n=1}^{N} \frac{s^2 \omega_n^2 V_n}{s^2 + 2s\omega_n \xi_n + \omega_n^2} \vartheta_{i,n}^2}, \tag{19}$$

where $X_i$, $F_i$, $\Lambda_i, \Omega_i$ and $\vartheta_{i,n}$ are the $i$-th element of $\mathbf{X}$, $\mathbf{F}$, $\boldsymbol{\Lambda}, \boldsymbol{\Omega}$ and $\boldsymbol{\theta}_n$, respectively. It should be noted that this equation neglects the coupling among EDRBs. However, complex structures might involve increasing coupling, which would call for more meticulous consideration.

Since multiple HRs are coupled to the primary cavity, their mutual interaction complicates the design optimization. To streamline this process, an equivalent single HR model is derived by rewriting Eq. (19) as:

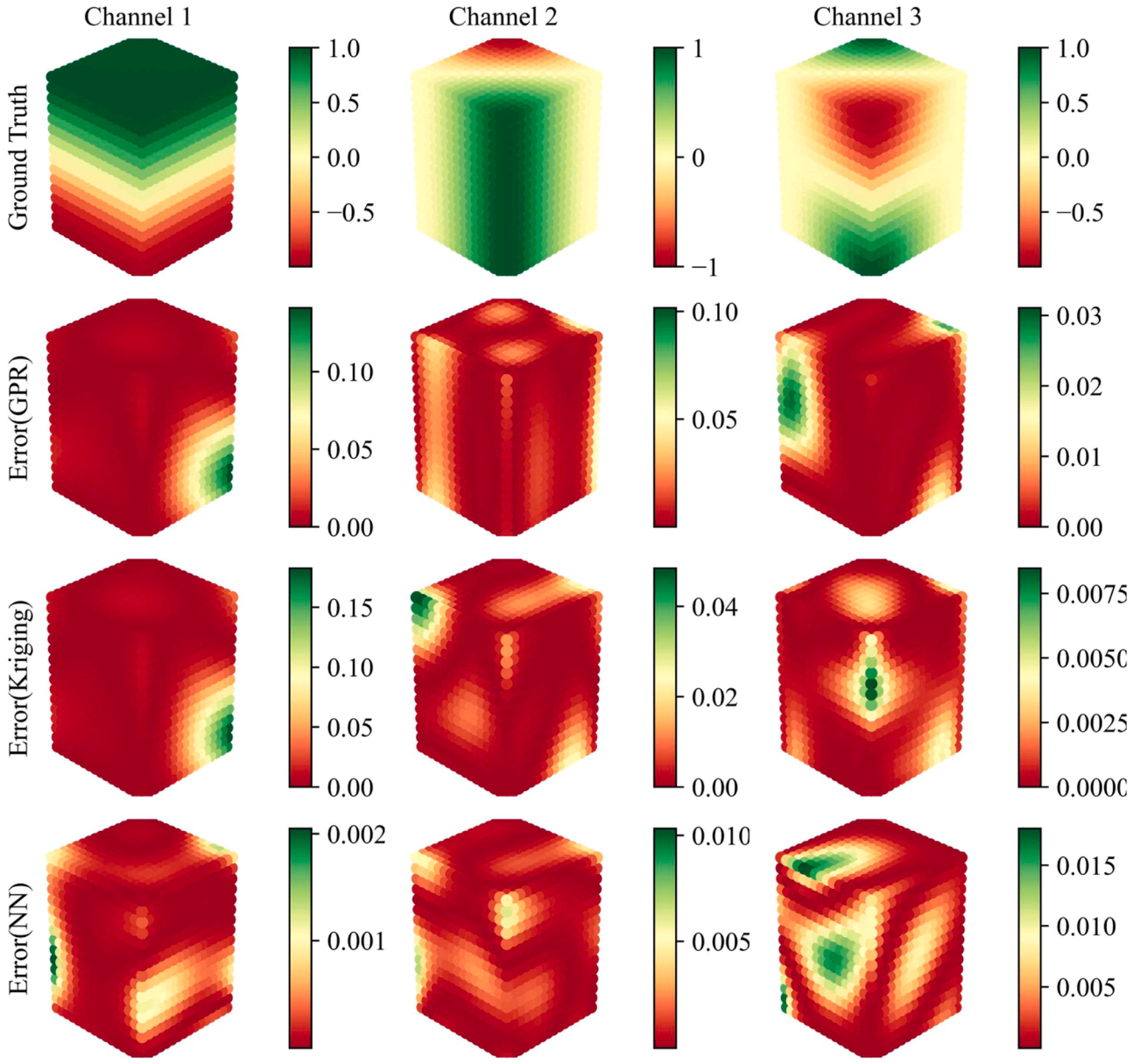



**Fig. 6.** Reconstruction errors of the physics-informed PINN (trained via ConFIG) compared with those of traditional purely data-driven methods, namely Kriging interpolation and Gaussian process regression (GPR). The results demonstrate that incorporating physical constraints from the homogeneous Helmholtz equation enhances reconstruction accuracy.

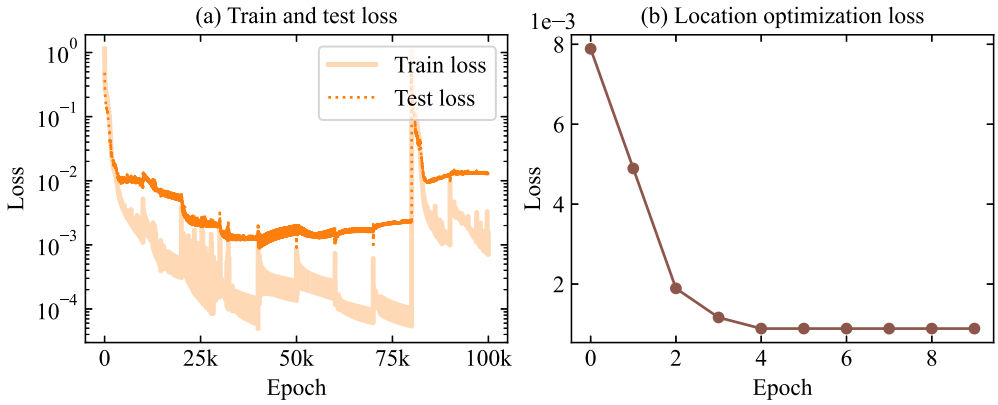



**Fig. 7.** Training and testing losses during the bi-level sensor placement optimization. The outer-loop optimization comprises 10 iterations, with the inner-loop PINN trained for 10,000 epochs per iteration. (a) shows the loss profiles across all 10 × 10,000 optimization steps; (b) presents the minimum loss achieved at the end of each outer-loop iteration.

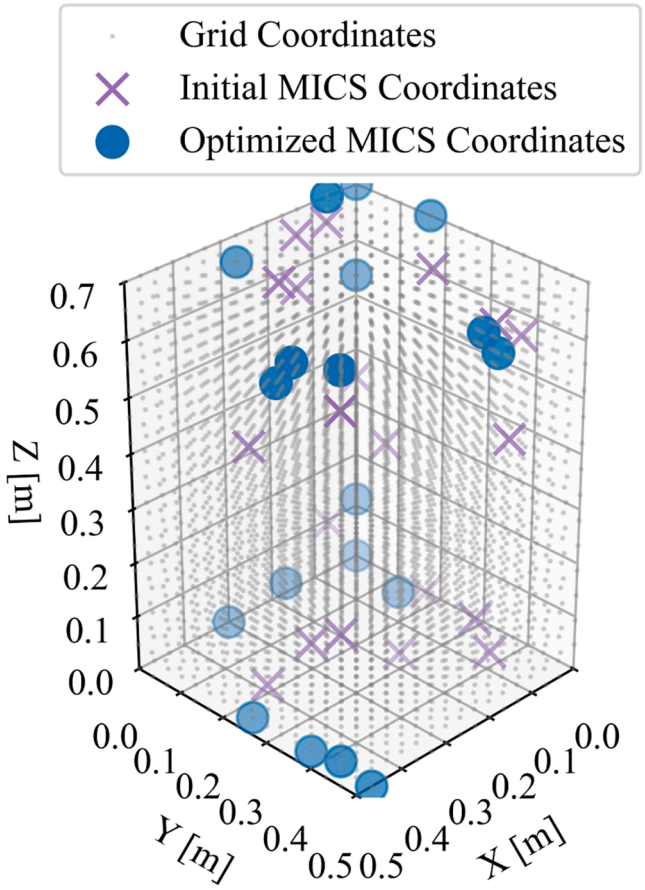



**Fig. 8.** Spatial distribution of microphones before and after sensor placement optimization. The optimized sensors exhibit strategic clustering near the corners, which correspond to acoustic pressure anti-nodes.

$$H_i = \frac{1}{\vartheta_{i,n}^2} \frac{1}{s^2 \Lambda_i^{\text{eff}} + K_i^{\text{eff}} + \frac{s^2 \omega_n^2 V_n}{s^2 + 2s\omega_n \xi_n + \omega_n^2}}, \tag{20}$$

where

$$\Lambda_i^{\text{eff}} = \frac{\Lambda_i + \sum_{m=1, m\neq n}^{N} \frac{\omega_m^2 V_m \vartheta_{i,m}^2}{s^2 + 2s\omega_m \xi_m + \omega_m^2}}{\vartheta_{i,n}^2}, K_i^{\text{eff}} = \frac{K_i}{\vartheta_{i,n}^2}, \Omega_i^{\text{eff}} = \sqrt{\frac{K_i^{\text{eff}}}{\Lambda_i^{\text{eff}}}}. \tag{21}$$

In Eq. (21), $\Lambda_i^{\text{eff}}$ is a frequency-dependent function involving unknown design parameters $\omega_m$ and $\xi_m$, rendering direct analytical treatment intractable. To simplify the design, two assumptions are made: (i) Frequency-independent approximation: coupling from other HRs ($m \neq n$) is treated as constant by setting $\omega = \Omega_i$ during the design of the $n$-th HR for the $i$-th EDRB. (ii) Elimination of unknown parameters: given the small equivalent volume ratio $\mu \ll 1$ (Eq. (23)), $\Lambda_i^{\text{eff}}$ is approximated by enforcing $\omega_m = \Omega_j$ and $\xi_m = 0$ when the $m$-th HR targets the $j$-th EDRB. These assumptions decouple the residual degrees of freedom while retaining their dynamic influence, as numerically verified in Appendix A. As a result, the system is reduced to an equivalent two-degree-of-freedom model, conducive to fixed-point theory analysis. Notably, the underlying assumptions and the proposed analytical optimization remain valid provided that the total volume of the installed HRs does not exceed 5% of the primary cavity volume. Should this volume ratio exceed this threshold, the HR design must account for the resulting alterations in the acoustic boundary conditions, necessitating iterative numerical updates or coupled structural-acoustic parameter optimization.

Accordingly, the normalized frequency response of Eq. (20) can be expressed as

$$H_i K_i = \frac{-\lambda^2 + \gamma^2 + 2\lambda\gamma j\xi_n}{\left(-\lambda^2 + \gamma^2\right)\left(-\lambda^2 + 1\right) - \lambda^2\gamma^2\mu + 2\lambda\gamma\left(-\lambda^2 + 1\right)j\xi_n}, \tag{22}$$

where

$$\lambda = \frac{\omega}{\Omega_i^{\text{eff}}}, \gamma = \frac{\omega_n}{\Omega_i^{\text{eff}}}, \mu = \frac{V_n}{\Lambda_i^{\text{eff}}}. \tag{23}$$

Under fixed-point theory, the frequency response function governed by Eq. (22) exhibits two invariant points, denoted as $\lambda_p$ and $\lambda_q$, which are independent of the damping ratio $\xi_n$. The coordinates of these points are obtained by solving

$$\frac{-\lambda^2 + \gamma^2}{\left(-\lambda^2 + \gamma^2\right)\left(-\lambda^2 + 1\right) - \lambda^2\gamma^2\mu} = -\frac{1}{-\lambda^2 + 1}, \tag{24}$$

which yields the squared frequency ratios of the two fixed points

$$\lambda_{p,q}^2 = \frac{(2 + 2\gamma^2 + \gamma^2\mu) \pm \sqrt{(2 + 2\gamma^2 + \gamma^2\mu)^2 - 16\gamma^2}}{4}. \tag{25}$$

The primary objective is to equalize the response amplitudes at the two invariant points by optimally tuning the frequency ratio $\gamma$. Based on Eq. (24), this optimization condition yields:

$$\frac{1}{-\lambda_p^2 + 1} = -\frac{1}{-\lambda_q^2 + 1}. \tag{26}$$

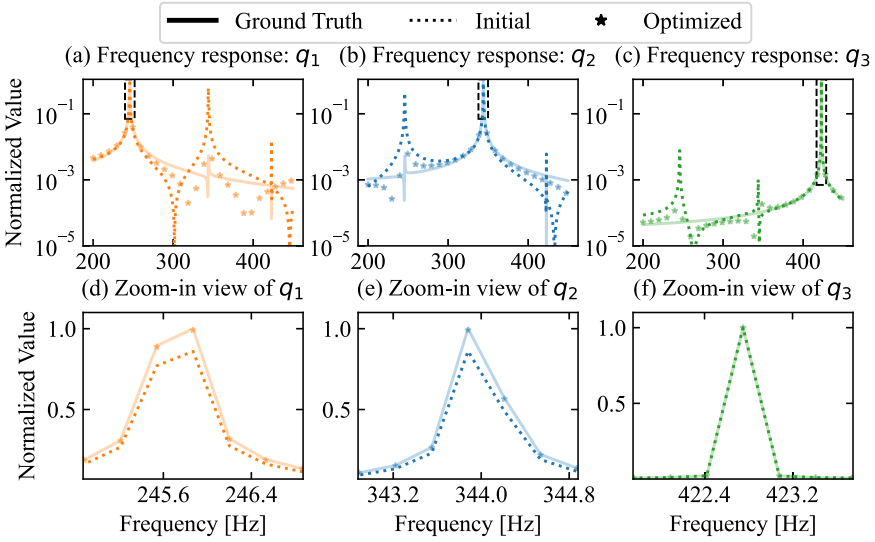



**Fig. 9.** Comparison of frequency-dependent components $\boldsymbol{q}_i(s)$ identified using the initial and optimized configurations. The ground truth is represented by solid lines, results from the initial configuration are shown as dotted lines, and those from the optimized configuration are depicted as scatter points.

Substituting Eq. (25) into Eq. (26) yields the expression for the optimal frequency ratio

$$\gamma_{opt} = \sqrt{\frac{2}{2+\mu}}. \tag{27}$$

Subsequently, the optimal damping ratio is determined by enforcing that the response amplitudes at the two invariant points correspond to the local maxima of the frequency response function. Mathematically, this condition is met when the first derivative of the response with respect to frequency at these points equals zero, namely

$$\frac{\partial (H_i K_i)^2}{\partial \lambda^2} = 0. \tag{28}$$

Substituting Eqs. (25) and (27) into Eq. (28) allows for the determination of two distinct damping ratios, $\xi_p$ and $\xi_q$. As these conditions cannot be satisfied simultaneously by a single value, the root-mean-square of $\xi_p$ and $\xi_q$ is selected as the optimal damping ratio to minimize the overall maximum response, yielding

$$\xi_{opt} = \sqrt{\frac{\xi_p^2 + \xi_q^2}{2}}, \tag{29}$$

where

$$\begin{aligned} \xi_p^2 &= \frac{\mu(a+\mu)}{8(\mu+2)(b+\mu)} + \frac{\sqrt{\frac{\mu^3 \cdot (46\mu + (\mu+2)(17\mu+32c)+16)}{\mu+2}}}{8(d+2\mu)}, \\ \xi_q^2 &= \frac{\mu(a-\mu)}{8(\mu+2)(b-\mu)} + \frac{\sqrt{\frac{\mu^3 \cdot (46\mu + (\mu+2)(17\mu-32c)+16)}{\mu+2}}}{8(d-2\mu)}, \end{aligned} \tag{30}$$

and

$$\begin{aligned} a &= \mu\sqrt{\frac{\mu}{\mu+2}} + 2\sqrt{\frac{\mu}{\mu+2}}, \quad b = \mu\sqrt{\frac{\mu}{\mu+2}} + \sqrt{\frac{\mu}{\mu+2}} \\ c &= 2\mu\sqrt{\frac{\mu}{\mu+2}} + \sqrt{\frac{\mu}{\mu+2}}, \quad d = 3\mu\sqrt{\frac{\mu}{\mu+2}} + 2\sqrt{\frac{\mu}{\mu+2}} \end{aligned}. \tag{31}$$

As demonstrated above, the resonant frequencies and damping ratios of the HRs can be analytically determined once their volumes are specified. These parameters directly govern the noise suppression level. Therefore, to determine the appropriate HR volumes, specific noise control targets must be predefined. To the best of the authors' knowledge, no explicit analytical relationship currently exists to guide HR volume selection based on prescribed noise control target, a gap that the remainder of this section aims to address.

The root-mean-square (RMS) acoustic pressure within the cavity is given by:

$$p_{RMS} = \sqrt{\frac{\sum_{n=1}^{N_d} p_n^2}{N_d}}, \tag{32}$$

where $N_d$ is the number of measurement points. Substituting Eq. (13) into Eq. (32) yields

$$p_{RMS} = \sqrt{\frac{\mathbf{X}^{\mathrm{H}} \boldsymbol{\Lambda} \boldsymbol{X}}{V}}, \tag{33}$$

where

$$\boldsymbol{\Lambda} = \Delta V \times \mathbf{U}^{\mathrm{H}}\mathbf{U}, \ V = \Delta V \times N_d, \tag{34}$$

where $\Delta V$ represents the volume of the sampling unit and $V$ is the total volume of the primary cavity. To characterize the resonant response associated with the $i$-th EDRB, Eq. (32) is reformulated as

$$p_{RMS} = \sqrt{\frac{X_i^2 \Lambda_i}{V}}. \tag{35}$$

Based on Eq. (22), the maximum normalized magnitude of the frequency response is given by

$$H_i K_i|_{max} = \frac{1}{-\lambda_p^2 + 1}. \tag{36}$$

Substituting Eqs. (25) and (27) into the preceding equation yields the following expression for the maximum response

$$X_i^2|_{max} = \frac{F_i^2}{K_i^2} \frac{2+\mu}{\mu}. \tag{37}$$

This section details the procedure for determining HR volumes based on prescribed noise control targets. Assume the HR is designed such that the maximum magnitude of the resonant response for the $i$-th EDRB satisfies $p_{RMS}|_{\max} = \sqrt{T_i}$. Based on Eqs. (35) and (37), the following relationship holds

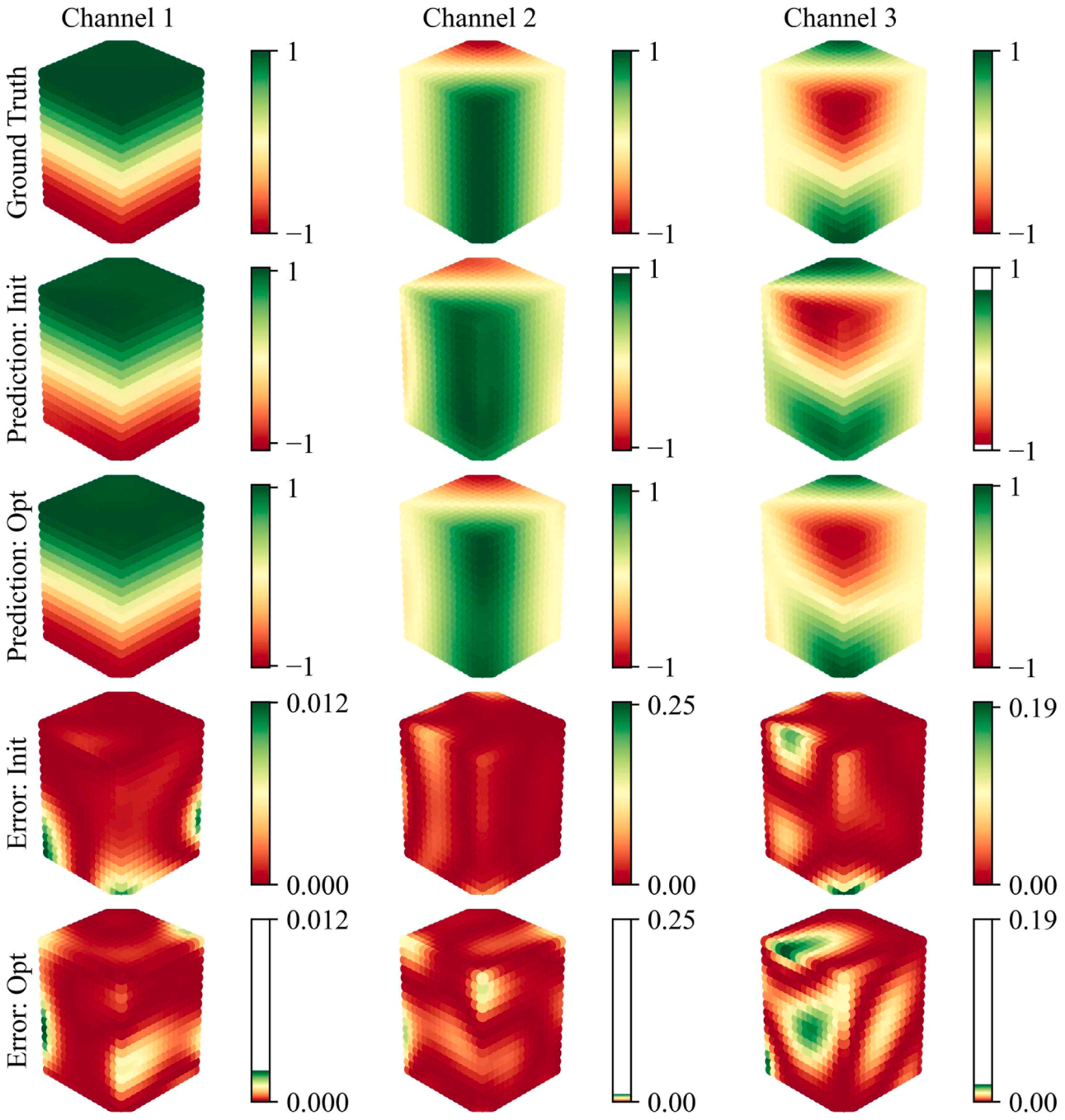



**Fig. 10.** Comparison of spatial components $\phi_i(\mathbf{r})$ (normalized pressure fields) reconstructed using the initial and optimized configurations. The corresponding squared error distributions are also presented.

$$p_{RMS}|_{\max} = \sqrt{\frac{F_i^2}{K_i^2}\frac{2+\mu}{\mu}\frac{\Lambda_i}{V}} = \sqrt{T_i}. \tag{38}$$

Substituting Eqs. (21) and (23) into this equation yields

$$\left(\frac{VK_i^2\vartheta_{i,n}^2 T_i}{F_i^2\Lambda_i} - \vartheta_{i,n}^2\right)V_n - \sum_{m=1,\ m\neq n}^{N}\frac{2\Omega_m^2\vartheta_{i,m}^2 V_m}{-\Omega_i^2+\Omega_m^2} - 2\Lambda_i = 0, \tag{39}$$

in which the unknown parameter $F_i$ can be determined through the following optimization process

$$\underset{F_i}{\operatorname{argmin}}\|X_i - \frac{F_i}{\left[s^2+(\Omega_i)^2\right]\Lambda_i}\|_2, \tag{40}$$

where $X_i$ is experimentally determined via Eqs. (13) and (18), while the resonant frequency $\Omega_i$ is identified from the resonant peak of the cavity response.

For $N$ HRs, $N$ equations can be obtained, expressed as

$$\begin{bmatrix} V_1 \\ \vdots \\ V_N \end{bmatrix} = 2\begin{bmatrix} \frac{VK_1^2\vartheta_{1,1}^2 T_1}{F_1^2\Lambda_1} - \vartheta_{1,1}^2 & \cdots & -\frac{2\Omega_N^2\vartheta_{1,N}^2}{-\Omega_1^2+\Omega_N^2} \\ \vdots & \ddots & \vdots \\ -\frac{2\Omega_1^2\vartheta_{N,1}^2}{-\Omega_N^2+\Omega_1^2} & \cdots & \frac{VK_N^2\vartheta_{N,N}^2 T_N}{F_N^2\Lambda_N} - \vartheta_{N,N}^2 \end{bmatrix}^{-1}\begin{bmatrix} \Lambda_1 \\ \vdots \\ \Lambda_N \end{bmatrix}. \tag{41}$$

Solving this linear equation directly provides the volume distribution required to meet the prescribed attenuation targets. This analytical

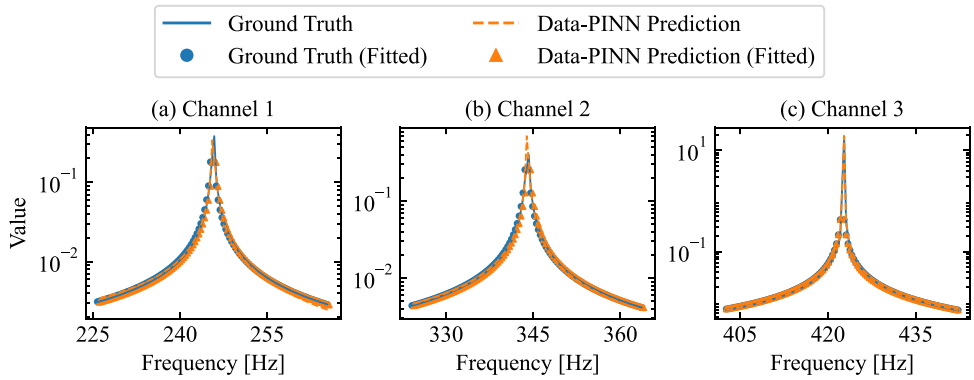



**Fig. 11.** Identification of the generalized force via curve fitting based on Eq. (40). The curves extracted from the pressure field are represented by solid lines, while the corresponding fitted results are indicated by scatter points. A comparison between results derived from the ground truth and those obtained from the reconstructed acoustic pressure field is presented to validate the identification accuracy.

**Table 2**
Optimal design specifications for HRs: comparison of parameters (resonant frequency $\omega_n$, damping ratio $\xi_n$, volume $V_n$) designed from ground-truth pressure field versus those obtained from the reconstructed pressure field.

| | | Volume [$m^3$] | | Frequency [Hz] | | Damping ratio | |
|---|---|---|---|---|---|---|---|
| | | GT | NN | GT | NN | GT | NN |
| Target I | HR1 | $5.7 \times 10^{-5}$ | $5.5 \times 10^{-5}$ | 245.5 | 245.8 | 0.015 | 0.015 |
| | HR2 | $1.5 \times 10^{-5}$ | $1.5 \times 10^{-5}$ | 344.0 | 344.3 | 0.011 | 0.011 |
| | HR3 | $7.8 \times 10^{-6}$ | $7.9 \times 10^{-6}$ | 422.6 | 422.6 | 0.011 | 0.011 |
| Target II | HR1 | $1.8 \times 10^{-4}$ | $1.7 \times 10^{-4}$ | 245.4 | 245.7 | 0.027 | 0.027 |
| | HR2 | $1.5 \times 10^{-5}$ | $1.5 \times 10^{-5}$ | 344.5 | 344.9 | 0.011 | 0.011 |
| | HR3 | $2.5 \times 10^{-6}$ | $2.5 \times 10^{-6}$ | 423.2 | 423.0 | 0.006 | 0.006 |
| Target III | HR1 | $1.8 \times 10^{-5}$ | $1.7 \times 10^{-5}$ | 245.5 | 245.8 | 0.009 | 0.008 |
| | HR2 | $1.5 \times 10^{-5}$ | $1.5 \times 10^{-5}$ | 343.6 | 344.0 | 0.011 | 0.011 |
| | HR3 | $2.5 \times 10^{-5}$ | $2.5 \times 10^{-5}$ | 422.4 | 422.4 | 0.019 | 0.020 |

design framework, fed exclusively by the reconstructed field, eliminates the need for analytical acoustic model or dense measurements, establishing a reconstruction-driven paradigm for passive acoustic control inside acoustic enclosures.

## 3. Numerical validation and discussions

This section presents a systematic numerical validation of the proposed hybrid Data-PINN framework using a canonical rectangular acoustic cavity. The validation follows a systematic pipeline: (i) benchmarking gradient-alignment strategies to resolve multi-objective training conflicts; (ii) optimizing discrete sensor placement to maximize reconstruction fidelity; (iii) quantifying the accuracy of reconstruction; and (iv) executing the design of HR to achieve effective noise control. The computational model considers a rectangular cavity ($0.5 \times 0.5 \times 0.7$) m excited by a unit point source at the origin corner (0,0,0) m. Acoustically rigid boundary conditions are imposed on all six walls to establish an analytical acoustic model.

### 3.1. Gradient alignment and optimization algorithm benchmarking

Given the dual-loss architecture of the hybrid Data-PINN (data fidelity and PDE residual), gradient conflicts during backpropagation can severely impede convergence. To address this, four optimization strategies are benchmarked: the Adam optimizer updates the PINN parameters using a linear combination $\mathscr{G}(\mathbf{g}_{\text{data}}, \mathbf{g}_{\text{PDE}}) = \mathbf{g}_{\text{data}} + \alpha \mathbf{g}_{\text{PDE}}$. In contrast, the ConFIG method [105] leverages orthogonal components of each individual loss gradient to ensure gradient alignment across all loss components, as detailed in Eq. (7). The IMTL-G method [106] rescales these gradients to equalize the projection of the final gradient onto each constituent loss gradient $\mathscr{G}(\mathbf{g}_{\text{data}}, \mathbf{g}_{\text{PDE}}) = (1-\alpha)\mathbf{g}_{\text{data}} + \alpha \mathbf{g}_{\text{PDE}}$. The PCGrad method [107] functions by projecting conflicting gradients onto the normal plane of the other gradient whenever their dot product is negative $\mathscr{G}(\mathbf{g}_{\text{data}}, \mathbf{g}_{\text{PDE}}) = \mathscr{O}(\mathbf{g}_{\text{data}}, \mathbf{g}_{\text{PDE}}) + \alpha \mathscr{O}(\mathbf{g}_{\text{PDE}}, \mathbf{g}_{\text{data}})$. The four optimization strategies employ identical PINN architecture and hyperparameter configuration, as detailed in Table 1.

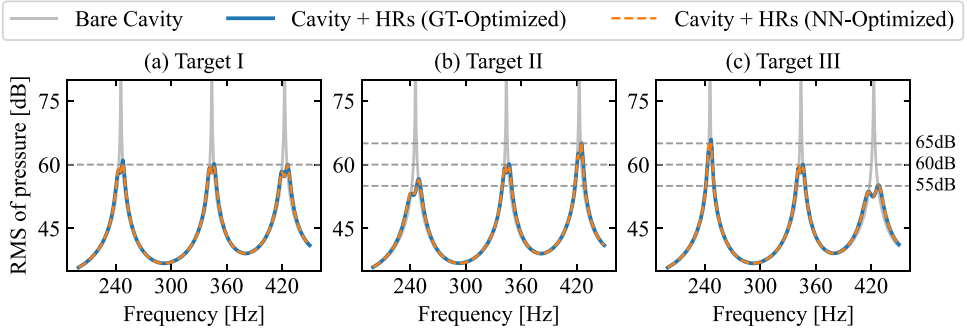



**Fig. 12.** Root mean square (RMS) acoustic pressure in the cavity: before HR installation (gray solid line); after installing HRs designed from ground truth (cyan solid line); and after installing HRs designed from reconstructed acoustic pressure field (orange dashed line). (a) Target I: equal peaks; (b) Target II: increasing peak levels from 55, 60 to 65 dB; (c) Target III: decreasing peak levels from 65, 60 to 55 dB.

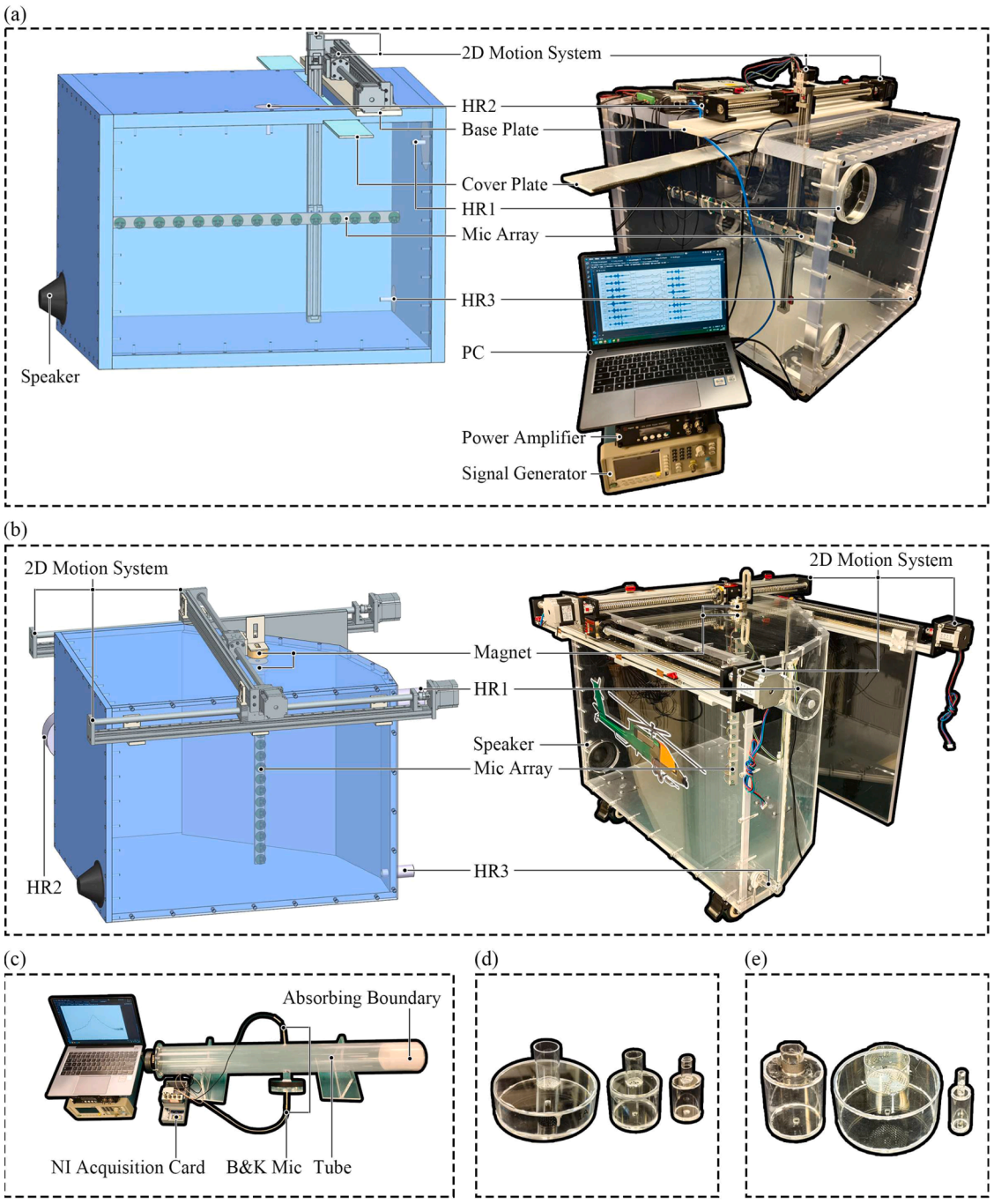



**Fig. 13.** Experimental setups and hardware configurations. (a) Test platform for the rectangular cavity; (b) experimental assembly for the helicopter cabin mockup; (c) impedance tube used for characterizing HR parameters; (d, e) fabricated HR prototypes used in the respective experiments.

Fig. 3 illustrates the mean squared error (MSE) of the reconstructed sound field as a function of the number of sparse microphones, while Fig. 4 presents the corresponding training and testing loss trajectories.

The results show that with only 8 microphones, all methods exhibit overfitting, characterized by divergent training and testing losses. Increasing the number of sensors to 27 substantially stabilizes PINN training and reduces the reconstruction error. However, further increases to 64 and 125 microphones yield only marginal improvements in fidelity, indicating diminishing returns relative to the added computational and experimental overhead. Consequently, 20 microphones are selected as the optimal trade-off between experimental feasibility and reconstruction accuracy. Furthermore, the training and testing loss trajectories for the 20-microphone configuration across different optimization algorithms are illustrated in Fig. 5.

Among the benchmarked algorithms, ConFIG consistently achieves the lowest testing loss and exhibits the most stable convergence profile. Therefore, ConFIG is adopted as the primary optimization strategy in subsequent analyses. Additionally, the proposed method is compared with traditional spatial interpolation techniques, namely Kriging interpolation and Gaussian process regression (GPR). Though widely used for field reconstruction, these methods rely purely on data-driven spatial correlations with no physical constraints. Fig. 6 shows that the PINN, constrained by the homogeneous Helmholtz equation and trained via ConFIG, outperforms these purely data-driven baselines in reconstruction accuracy.

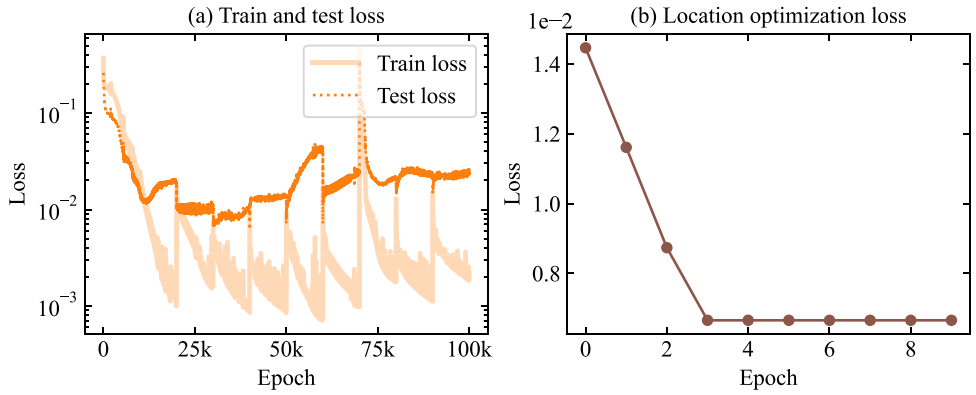



**Fig. 14.** Training and testing losses during the bi-level sensor placement optimization. The outer-loop optimization comprises 10 iterations, with the inner-loop PINN trained for 10,000 epochs per iteration. (a) shows the loss profiles across all 10 × 10,000 optimization steps; (b) presents the minimum loss achieved at the end of each outer-loop iteration.

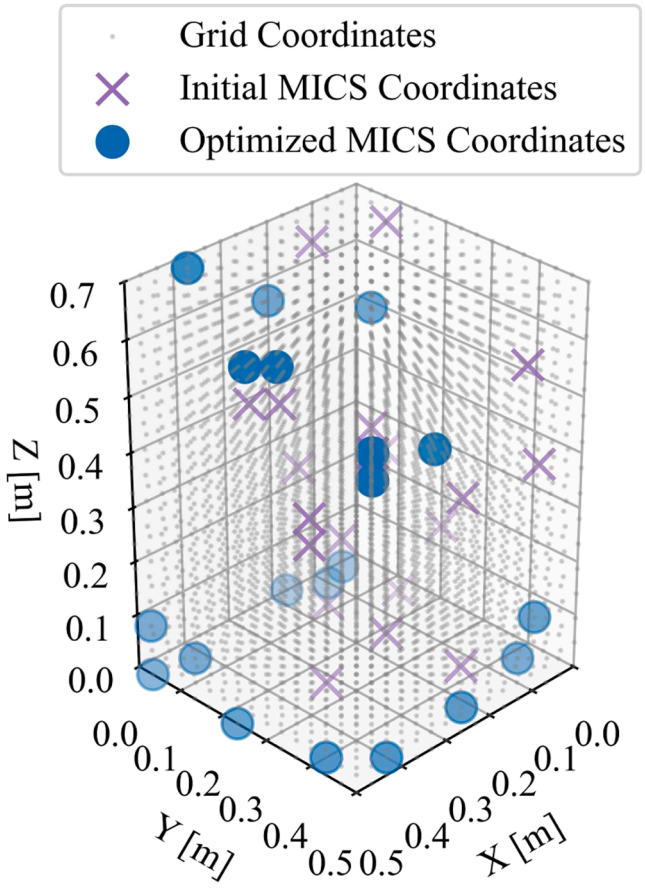



**Fig. 15.** Spatial distribution of microphones before and after sensor placement optimization. Consistent with numerical predictions, the optimized sensor locations remain strictly confined to the predefined discrete grid.

### 3.2. Bi-level discrete sensor placement optimization

With the number of microphones fixed at 20, the bi-level optimization framework (Fig. 1) is deployed to determine their optimal spatial configuration within a 16 × 16 × 16 uniform discretization grid. The outer loop iteratively updates sensor coordinates over 10 cycles, while the inner loop trains the PINN for 10,000 epochs per iteration. To mitigate entrapment in local optima, a random restart mechanism is triggered if the test loss stagnates for more than three consecutive outer-loop iterations. This strategy effectively improves the global search capacity of the algorithm, ensuring a more robust exploration of the discrete sensor configuration space.

The resulting loss evolution is depicted in Fig. 7. Fig. 7(a) captures the full optimization trajectory across all 10 × 10,000 steps, while Fig. 7 (b) highlights the minimum loss achieved for each outer-loop cycle. The optimization converges rapidly, with significant loss reduction occurring within the first four cycles. The abrupt loss increase observed at the 80,000-th epoch corresponds to the triggered random restart. This proposed discrete sensor placement optimization strategy ensures that sensor placement is optimized strictly within the physically realizable discrete grid, thereby avoiding the impractical continuous coordinates often yielded by differentiable search methods.

### 3.3. Reconstruction fidelity and physical interpretation

The spatial distributions of the initial random and optimized microphone configurations are compared in Fig. 8. Both configurations adhere strictly to the discretized mounting grid, confirming the practical viability of the placement strategy. Notably, the optimized sensors exhibit strategic clustering near coordinates (0.5,0.5,0) m, (0.5,0.5,0.7) m, and the corners near (0,0,0) m and (0,0,0.7) m. These locations correspond to acoustic pressure anti-nodes and structural boundaries where the local pressure energy density is maximized. Physically, this configuration inherently enhances the signal-to-noise ratio for extracting frequency-dependent components $q_i(s)$, while simultaneously providing the PINN with sufficient spatial observability to reconstruct the global pressure distribution $\phi_i(\mathbf{r})$.

The accuracy of the decomposed components is quantified in Fig. 9 and Fig. 10. Fig. 9 demonstrates that the optimized placement substantially improves the identification of the frequency-dependent components $q_i(s)$, with the reconstructed spectral peaks closely aligning with ground-truth values across the target bandwidth. Fig. 10 further validates the spatial reconstruction, showing that the optimized configuration yields a marked reduction in squared error. By synthesizing $q_i(s)$ and $\phi_i(\mathbf{r})$ via Eq. (2), the framework achieves high-fidelity full-field pressure reconstruction from only 20 sparse measurements, establishing a reliable foundation for the subsequent noise control design.

### 3.4. Reconstruction-driven HR design for noise suppression

Leveraging the reconstructed pressure field, the noise control design procedure detailed in Section 2.2 is executed to analytically determine the optimal HR parameters. The generalized force term, a critical input for volume calculation, is identified through curve-fitting the relationship defined in Eq. (40). Fig. 11 compares the spectral curves extracted from the reconstructed field (via Eqs. (13) and (18)) with the fitted results. The close agreement between the reconstructed data, the fitted

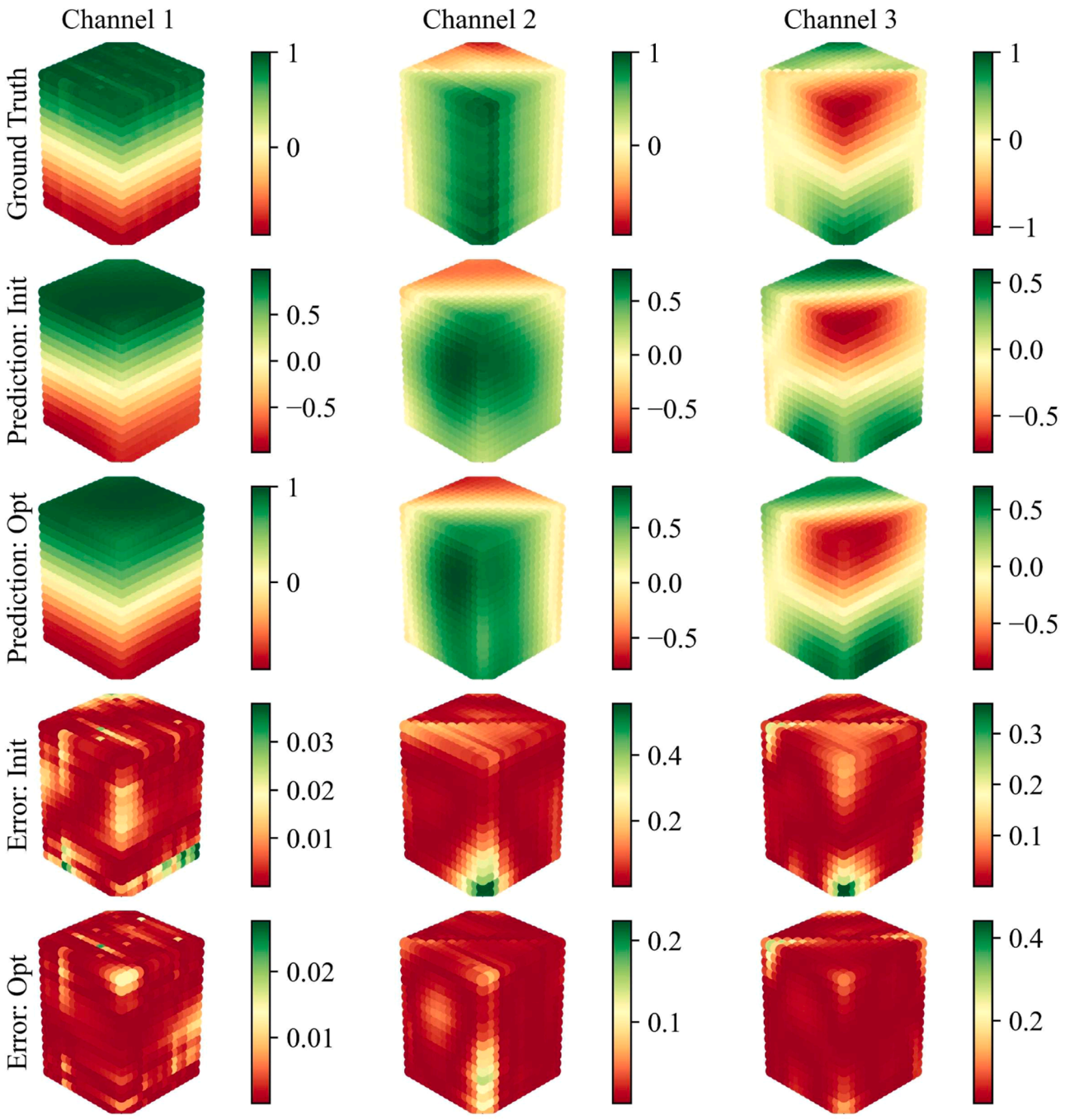



**Fig. 16.** Comparison of spatial components $\phi_i(\mathbf{r})$ reconstructed using the initial and optimized configurations. The corresponding squared error distributions are also presented.

curves, and the ground truth confirms that the reconstructed field preserves the essential spectral and spatial characteristics required for accurate HR design, despite the severe data sparsity.

Using the identified parameters, the optimal resonant frequencies, damping ratios, and volumes for three HRs are computed analytically using Eqs. (27), (29) and (41) to meet three distinct and prescribed noise control targets. The resulting specifications are summarized in Table 2, which directly compares the ground-truth-based (GT) and reconstruction-driven (NN) designs. Across all targets, the NN-optimized parameters exhibit minor deviations relative to the GT benchmarks. This close agreement validates the effectiveness of the proposed reconstruction-driven design methodology, confirming that sparse-measurement-based field reconstruction can reliably support analytical HR design by following the procedure established in this paper.

The final validation step integrates the analytically designed HRs into the numerical cavity model to evaluate their noise suppression performance. Fig. 12 presents the RMS acoustic pressure spectra before and after HRs' installation for all three targets. The gray solid line represents the baseline cavity response, while the cyan and orange curves correspond to the GT-based and NN-based HR designs, respectively. The results confirm that both design approaches achieve effective noise suppression, with the NN-derived HRs delivering attenuation performance closely comparable to that of the GT benchmark. This numerical validation demonstrates that the proposed framework successfully bridges sparse acoustic sensing, physics-informed field reconstruction,

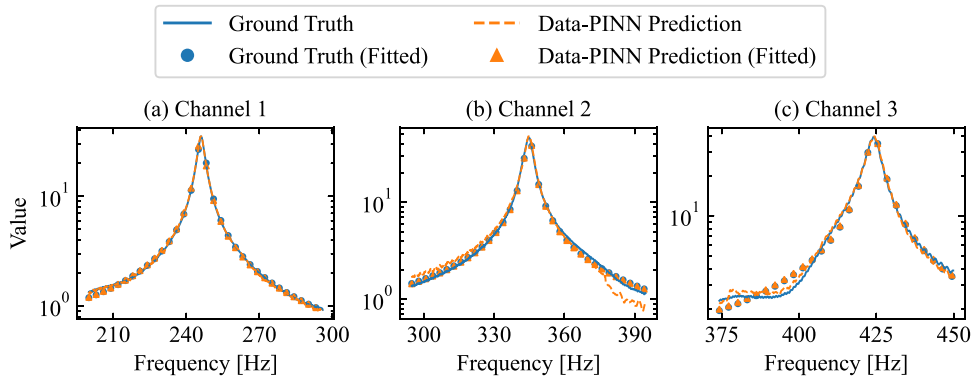



**Fig. 17.** Identification of the generalized force via curve fitting based on Eq. (40). The curves extracted from the pressure field are represented by solid lines, while the corresponding fitted results are indicated by scatter points. A comparison between results derived from the ground truth and those obtained from the reconstructed acoustic pressure field is presented to validate the identification accuracy.

**Table 3**
Optimal design specifications for HRs: comparison of parameters designed from ground-truth pressure field versus those obtained from the reconstructed pressure field.

| | | Radius [mm] | Height [mm] | Frequency [Hz] | | Damping ratio | |
|---|---|---|---|---|---|---|---|
| | | | | Designed | Measured | Designed | Measured |
| HR1 | GT | 58 | 28 | 245.7 | 246.2 | 0.035 | 0.034 |
| | NN | | | 245.8 | 245.8 | 0.032 | 0.035 |
| HR2 | GT | 28 | 42 | 345.4 | 345.6 | 0.027 | 0.027 |
| | NN | | | 344.9 | 345.4 | 0.024 | 0.026 |
| HR3 | GT | 14.5 | 42 | 425.9 | 426 | 0.021 | 0.018 |
| | NN | | | 425.2 | 425.6 | 0.013 | 0.016 |

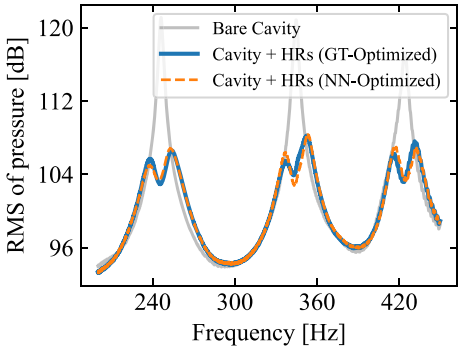



**Fig. 18.** Root mean square (RMS) acoustic pressure in the cavity: before HR installation (gray solid line); after installing HRs designed from ground truth (cyan solid line); and after installing HRs designed from reconstructed acoustic pressure field (orange dashed line).

and analytical absorber design, establishing a reconstruction-driven paradigm for passive noise control that operates exclusively on sparse measurements.

## 4. Experimental validation

This section presents two experimental studies to validate the efficacy and scalability of the proposed reconstruction-driven design framework. The first experiment employs a canonical rectangular cavity to quantify design accuracy, while the second investigates a helicopter cabin mockup to demonstrate the applicability of the proposed method to complex, arbitrarily shaped geometries. Both cases share similar measurement architecture, illustrated in Fig. 13, but differ in structural complexity and acoustic pressure distribution. The experimental protocol consistently follows a four-stage pipeline: (i) discrete sensor placement optimization; (ii) sparse-to-dense acoustic field reconstruction; (iii) analytical design of HRs and (iv) experimental validation of noise suppression performance. Furthermore, the equal-peak control target is selected as it represents the most widely adopted design criterion in practical noise control applications.

### 4.1. Validation on a rectangular cavity

The first experiment employs a rectangular cavity to validate the proposed reconstruction-driven design framework, as depicted in Fig. 13 (a). To facilitate sound field reconstruction from sparse measurements while enabling rigorous validation against dense ground-truth data, a three-dimensional acoustic scanning system was customized. This system integrates a linear MEMS microphone array with a dual-axis translation stage, allowing automated point-by-point pressure field measurement across the cavity volume. Acoustic excitation is generated by a loudspeaker driven by a signal generator and power amplifier, ensuring a high signal-to-noise ratio. The microphone responses are simultaneously acquired and recorded using a computer-based data acquisition system.

Guided by the methodology detailed in Section 2, the initial positions of the 20 microphones are randomly initialized within the discretized search space defined by the scanning grid. These coordinates are subsequently optimized using the proposed bi-level framework (Fig. 1). The training and testing loss trajectories, which illustrate the convergence behavior during the experimental optimization process, are plotted in Fig. 14. As shown, the outer-loop optimization successfully drives the reconstruction loss downward, experimentally validating the efficacy of the proposed bi-level sensor placement framework.

The spatial distribution of the microphones before and after optimization is compared in Fig. 15. Consistent with numerical predictions, the optimized sensor locations remain strictly confined to the predefined discrete grid, thereby demonstrating the practical viability of the discrete placement strategy. The reconstruction accuracy achieved with the optimized configuration is further quantified in Fig. 16, which shows

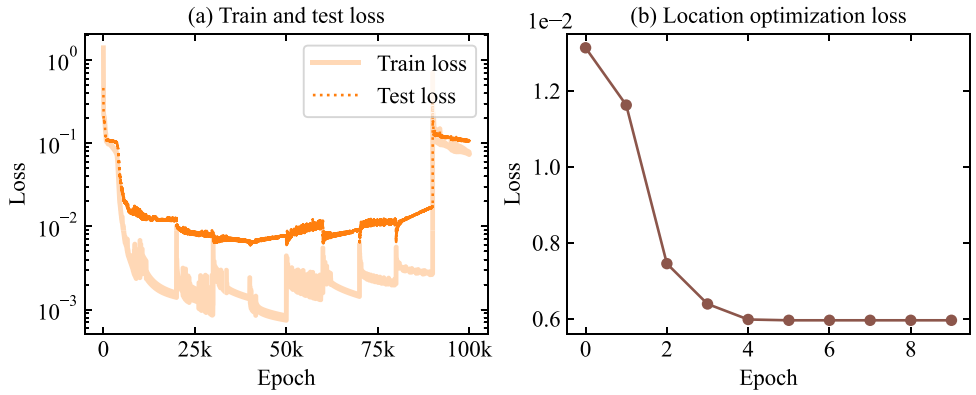



**Fig. 19.** Training and testing losses during the bi-level sensor placement optimization. The outer-loop optimization comprises 10 iterations, with the inner-loop PINN trained for 10,000 epochs per iteration. (a) shows the loss profiles across all 10 × 10,000 optimization steps; (b) presents the minimum loss achieved at the end of each outer-loop iteration.

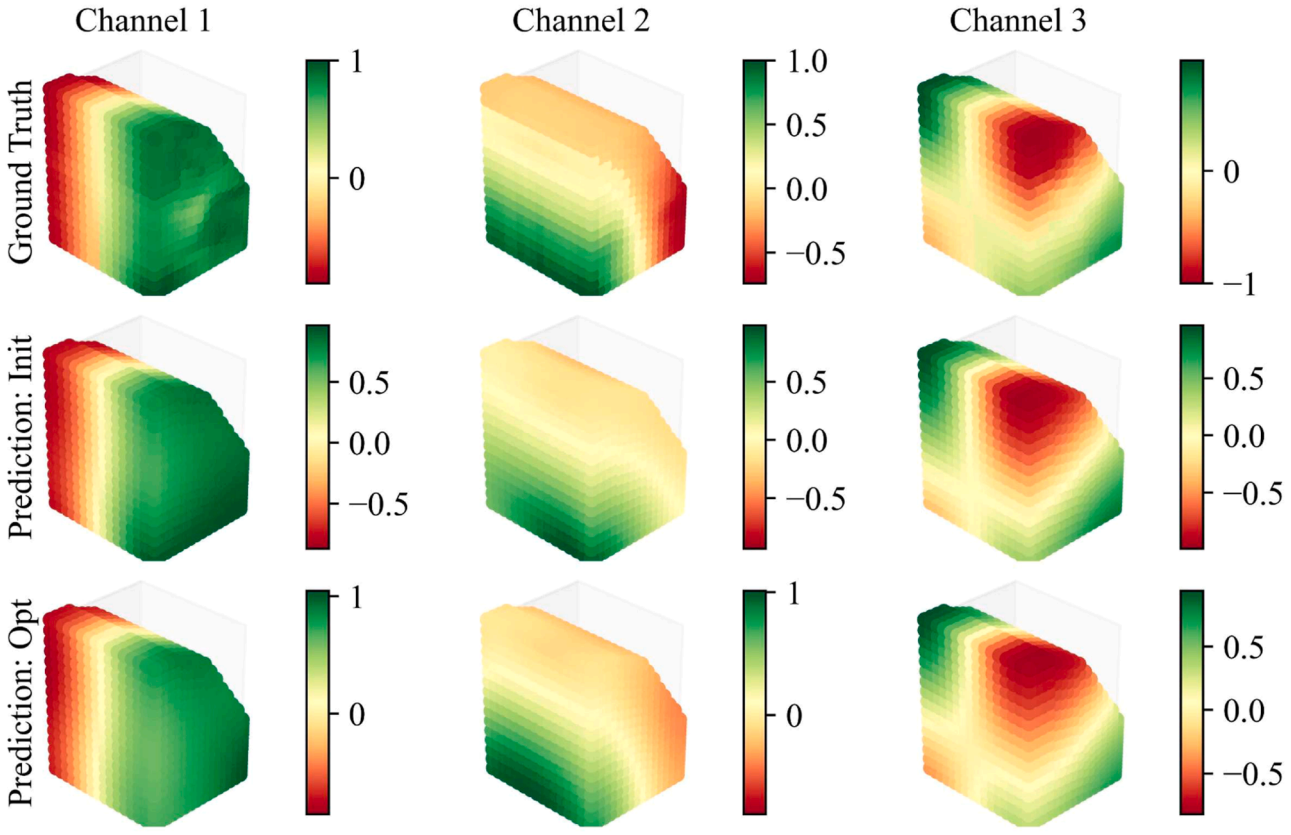



**Fig. 20.** Comparison of spatial components $\phi_i(\mathbf{r})$ reconstructed using the initial and optimized configurations. The improvement in field reconstruction fidelity demonstrates the robustness and scalability of the proposed method for complex, arbitrarily shaped geometries.

**Table 4**
Optimal design specifications for HRs: comparison of parameters designed from ground-truth pressure field versus those obtained from the reconstructed pressure field.

| | | Radius [mm] | Height [mm] | Frequency [Hz] | | Damping ratio | |
|---|---|---|---|---|---|---|---|
| | | | | Designed | Measured | Designed | Measured |
| HR1 | GT | 28 | 69 | 339.2 | 340.0 | 0.023 | 0.026 |
| | NN | | | 339.6 | 340.4 | 0.016 | 0.016 |
| HR2 | GT | 58 | 48 | 371.2 | 370.0 | 0.037 | 0.041 |
| | NN | | | 369.0 | 369.6 | 0.031 | 0.037 |
| HR3 | GT | 9.5 | 46 | 429.8 | 429.6 | 0.011 | 0.026 |
| | NN | | | 430.0 | 430.0 | 0.006 | 0.026 |

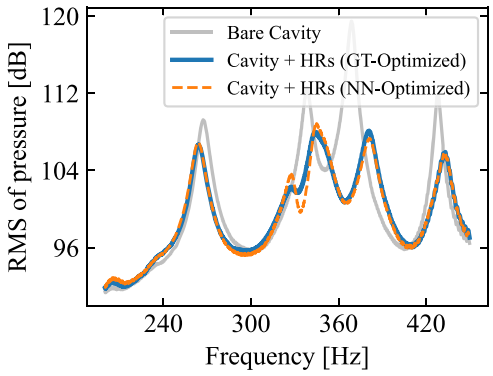



**Fig. 21.** Root mean square (RMS) acoustic pressure in the cavity: before HR installation (gray solid line); after installing HRs designed from ground truth (cyan solid line); and after installing HRs designed from reconstructed acoustic pressure field (orange dashed line).

a marked reduction in squared error compared to the random initialization.

Notably, the bi-level optimization is executed on a workstation equipped with an NVIDIA RTX 4070 Ti Super GPU, requiring a total training time of 21 min and 40 s. In contrast, acquiring the ground-truth dense measurement data in our experimental validation using the dual-axis translation stage took 134 min. Consequently, the proposed PINN-based framework reduces the overall workflow time by approximately 84%. More importantly, on top of the significant temporal advantage, the proposed method requires only 20 sparsely distributed microphones. This drastically reduces the hardware requirements and operational complexity, conducive to *in-situ* noise control design.

Following the full-field pressure reconstruction, the generalized force term is identified by curve-fitting the relationship defined in Eq. (40). Fig. 17 compares the spectral curves extracted from the reconstructed pressure field with the fitted results. The close alignment between the reconstructed data, fitted curves, and ground truth confirms that the PINN-reconstructed field preserves the essential spectral characteristics required for accurate HR design.

Using the identified parameters, the optimal HR parameters are analytically computed via Eqs. (27), (29) and (41). As shown in Fig. 13 (d), the HRs were fabricated from acrylic tubes, with the larger-diameter tube serving as the volume cavity and the smaller-diameter tube functioning as the neck, to which a perforated end plate was attached. Resonant frequencies were tuned by adjusting neck tube lengths, while damping ratios were controlled through the perforation ratio of the end plates. Prior to installation, each prototype was carefully characterized through impedance tube testing (Fig. 13(c)) to verify its acoustic impedance and resonance behavior, ensuring that manufacturing tolerances do not compromise theoretical performance. The designed and measured HR parameters are compared in Table 3.

Upon integration into the cavity, the noise suppression capability was evaluated by measuring the internal RMS acoustic pressure. The results, presented in Fig. 18, demonstrate that HRs designed from the reconstructed field achieve effective attenuation across all prescribed frequency bands. Their performance closely matches that of the ground-truth-based design, with a maximum deviation in peak attenuation of $<$1.6 dB. This experimental validation confirms that the proposed framework successfully bridges sparse sensing, physics-informed reconstruction, and analytical absorber design without requiring dense measurements or explicit source characterization.

### 4.2. Validation on a complex helicopter cabin mockup

To evaluate the scalability and robustness of the proposed framework in practical engineering scenarios, the second experimental study investigates a helicopter cabin mockup (Fig. 13(b)), which features complex and irregular internal volume. The measurement apparatus remains similar to the one used in rectangular cavity experiment, employing the linear MEMS microphone array, dual-axis translation stage, and data acquisition system. Acoustic excitation is similarly provided by a loudspeaker, installed at the cavity corner and driven by a signal generator and power amplifier.

Following the established protocol, 20 microphone positions are initially randomized within the discretized scanning grid and subsequently optimized using the bi-level framework. The convergence behavior of the training and testing losses throughout the optimization process is illustrated in Fig. 19. Despite the geometric complexity, the optimization algorithm successfully identifies sensor configurations that minimize the reconstruction error. The reconstruction accuracy of the optimized sensor layout is presented in Fig. 20, which demonstrates a substantial improvement in field reconstruction fidelity compared to the initial random placement.

Leveraging the reconstructed pressure field, the HR design procedure is executed to determine optimal HR parameters. The HRs were fabricated with the same methodology and pre-characterized via impedance tube measurements. The designed and measured HR parameters are compared in Table 4.

The resulting noise attenuation performance is illustrated in Fig. 21. The RMS acoustic pressure spectra confirm that the reconstruction-driven HRs achieve substantial broadband suppression. Furthermore, the peak attenuation values closely match those of the ground-truth-based design, with a maximum deviation of $<$2.6 dB.

This case study underscores a practical engineering advantage of the proposed methodology: it eliminates the dependency on analytical cavity models or dense three-dimensional scanning equipment, which are typically impractical in complex engineering structures. The framework established in this work operates exclusively on sparse measurements and embeds physical constraints directly into the reconstruction pipeline. Consequently, it delivers a robust, scalable, and model-free paradigm for passive noise control inside acoustic enclosures of arbitrary shape. The consistent performance across both canonical and highly irregular geometries validates its readiness for real-world deployment in aerospace, automotive, and architectural acoustics applications.

## 5. Conclusions

This study presents a hybrid Data-PINN framework for the reconstruction-driven design of HR in complex acoustic enclosures. To circumvent the reliance on accurate analytical models and the impracticality of dense three-dimensional pressure measurements, the proposed methodology integrates three core innovations:

(i) A spatial-frequency decomposition strategy decouples operational variations from stable spatial characteristics. This enables a PINN, constrained by a homogeneous Helmholtz equation, to reconstruct high-fidelity spatial fields from sparse data while avoiding source-term identification.
(ii) A bi-level discrete optimization architecture hierarchically determines optimal and physically realizable sensor placement. Within this architecture, the ConFIG gradient alignment algorithm ensures stable and conflict-free PINN training.
(iii) An analytical design approach leveraging EDRB decomposition and fixed-point theory to directly compute optimal HR parameters from the reconstructed full-field pressure.

Numerical simulations and experimental validations on both regular and irregular-shaped enclosures demonstrate that the proposed framework achieves accurate acoustic field reconstruction from sparse measurements and enables HR designs with noise suppression performance nearly identical to ground-truth-based approaches. By synergizing sparse sensing, physics-informed field reconstruction, and analytical HR

design, this work establishes a robust, model-free paradigm for passive noise control in practical engineering structures where conventional modeling and dense acoustic measurement are highly challenging.

## CRediT authorship contribution statement

**Hangxing Li:** Writing – original draft, Visualization, Validation, Software, Resources, Methodology, Formal analysis, Data curation, Conceptualization. **Yang Song:** Writing – review & editing, Methodology, Conceptualization. **Li Cheng:** Writing – review & editing, Writing – original draft, Visualization, Validation, Supervision, Project administration, Methodology, Funding acquisition, Conceptualization.

## Declaration of competing interest

The authors declare that they have no known competing financial interests or personal relationships that could have appeared to influence the work reported in this paper.

## Acknowledgment

The work was partially supported by a grant from the RIAIoT (Research Institute for Artificial Intelligence of Things) through project P0049625.

## Appendix A

These assumptions approximate the frequency-dependent function as a constant. To verify the validity of this simplification, the exact and approximated values of $\Lambda_i^{\text{eff}}$ are compared across the frequency range of interest, as illustrated in Fig. 22.

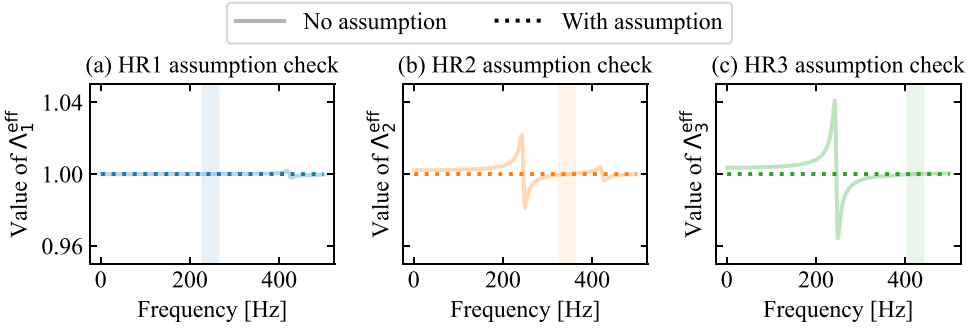



**Fig. 22.** Comparison of the exact and approximated values of $\Lambda_i^{\text{eff}}$ with and without the proposed assumptions. The shaded regions indicate the target frequency ranges of the corresponding HR designs.

The results demonstrate that within the target frequency band of each HR design (indicated by the shaded regions), the exact and approximated values of $\Lambda_i^{\text{eff}}$ agree well with each other. This validates the proposed simplifications, confirming that the HRs can be analytically designed with high fidelity despite the decoupling assumptions.

## Data availability

The code is available at GitHub: https://github.com/HengistLi/Hybrid-Data-PINN-Framework-for-Reconstruction-Driven-HR-Design.

## References

[1] Reitich-Stolero T, Aberg KC, Halperin D, Ariel C, Morris G, Goldstein L, et al. Rate and noise in human amygdala drive increased exploration in aversive learning. Nature 2025;646:883–92. https://doi.org/10.1038/s41586-025-09466-1.

[2] Shukla A, Tandel BN, Kajaliya PP. Auditory and mental well-being of teachers in urban noise environment: a partial least square structural equation model approach. Appl Acoust 2025;230:110417. https://doi.org/10.1016/j.apacoust.2024.110417.

[3] Aboutiman A, Maamoun KSA, Karimi HR, Ripamonti F. Hybrid deep learning–based active noise control for encapsulated structures with openings. Expert Syst Appl 2026;309:131247. https://doi.org/10.1016/j.eswa.2026.131247.

[4] Vazquez A, Garcia L, Avalos J-G, Sanchez G, Nakano M, Toscano K, et al. A high-precision multi-arithmetic neural circuit for the efficient computation of the new filtered-X kronecker product APL-NLMS algorithm applied to active noise control. Expert Syst Appl 2022;191:116255. https://doi.org/10.1016/j.eswa.2021.116255.

[5] Han J, Zhou J, Bu H. An ultra-thin acoustic metamaterial for low-frequency and broadband noise mitigation. Int J Mech Sci 2026;315:111428. https://doi.org/10.1016/j.ijmecsci.2026.111428.

[6] Zheng L, Zhou J, Guan Y. Ultrathin metaliner for dual suppression of broadband flow-induced noise and tonal thermoacoustic oscillations. Int J Mech Sci 2025;308:110988. https://doi.org/10.1016/j.ijmecsci.2025.110988.

[7] Lu J-H, Ding S, Zhou K, Ni Y-Q. Kolmogorov-arnold networks-optimized honeycomb acoustic metamaterials for railway noise control. Int J Mech Sci 2025;303:110672. https://doi.org/10.1016/j.ijmecsci.2025.110672.

[8] Zeng Q, Zhang W, Cheng B, Wang M, Zhang M, Tang S, et al. Low-frequency underwater wave absorption governed by dual-objective constrained deep neural network. Eur J Mech - ASolids 2026;120:106281. https://doi.org/10.1016/j.euromechsol.2026.106281.

[9] Cao F, Zeng Q, Xia Z, Wang M, Hou C, Li B, et al. Inverse design of bending channel sound-absorbing structures with porous material by two-stage deep neural network model. Phys Scr 2025;100:055963. https://doi.org/10.1088/1402-4896/adcd0d.

[10] Cao F, Cheng B, Tang L, Wang L, Liu K, Hou H. Sound absorption performance of helmholtz array with embedded rough necks and small back cavities based on weak coupling. Phys Scr 2025;100:125938. https://doi.org/10.1088/1402-4896/ae2979.

[11] Abbad A, Atalla N, Ouisse M, Doutres O. Numerical and experimental investigations on the acoustic performances of membraned helmholtz resonators embedded in a porous matrix. J Sound Vib 2019;459:114873. https://doi.org/10.1016/j.jsv.2019.114873.

[12] Mahesh K, Mini RS. Theoretical investigation on the acoustic performance of helmholtz resonator integrated microperforated panel absorber. Appl Acoust 2021;178:108012. https://doi.org/10.1016/j.apacoust.2021.108012.

[13] Gao N, Qu S, Li J, Wang J, Chen W. Harnessing post-buckling deformation to tune sound absorption in soft helmholtz absorbers. Int J Mech Sci 2021;208:106695. https://doi.org/10.1016/j.ijmecsci.2021.106695.

[14] Ning L, Wang Y-Z, Wang Y-S. Active control of elastic metamaterials consisting of symmetric double helmholtz resonator cavities. Int J Mech Sci 2019;153-154:287–98. https://doi.org/10.1016/j.ijmecsci.2019.02.007.

[15] Liu X, Wu JH, Niu J, Li W, Liu C. Vibro-acoustic helmholtz absorber with soft wall for broadband sound absorption. Int J Mech Sci 2025;289:110083. https://doi.org/10.1016/j.ijmecsci.2025.110083.

[16] Li D, Cheng L, Yu GH, Vipperman JS. Noise control in enclosures: modeling and experiments with T-shaped acoustic resonators. J Acoust Soc Am 2007;122:2615–25. https://doi.org/10.1121/1.2783122.

[17] Wu S, Li H. A data-driven design method of distributed dynamic vibration absorber for broadband vibration suppression of thin-walled structures. Thin-Walled Struct 2023;182:110264. https://doi.org/10.1016/j.tws.2022.110264.
[18] Li H, Wu S, Chen Q, Fei Q. Design of dynamic absorbers to control the flexural resonant vibration of structures characterized by multiple natural modes. J Sound Vib 2021;513:116415. https://doi.org/10.1016/j.jsv.2021.116415.
[19] Li H, Wong W, Cheng L. Model-free sequential design of absorbers for customized vibration control. Int J Mech Sci 2026;312:111280. https://doi.org/10.1016/j.ijmecsci.2026.111280.
[20] Liu Y, Li C, Lu S, Dong S, Fan S. Temperature-compensated high-sensitive graphene fabry–perot acoustic sensor. IEEE Trans Instrum Meas 2025;74:1–7. https://doi.org/10.1109/TIM.2025.3576026.
[21] Song C, Huang S, Ma H, Xie S, Tsai DP, Zhu J, et al. Self-powered frequency-selective acoustic sensor based on bound states in the continuum. Adv Sci 2025;12:2410379. https://doi.org/10.1002/advs.202410379.
[22] Wei X, Li A, Zhou J, Shao L, Zhang W. A calibration-free self-quadrature locked extrinsic fiber acoustic sensor with ultrahigh sensitivity. IEEE Trans Instrum Meas 2025;74:1–8. https://doi.org/10.1109/TIM.2024.3502737.
[23] Martin P, Rothberg SJ. Pseudo-vibration sensitivities for commercial laser vibrometers. Mech Syst Signal Process 2011;25:2753–65. https://doi.org/10.1016/j.ymssp.2011.02.009.
[24] Nozato H, Kokuyama W, Shimoda T, Inaba H. Primary calibration method for laser doppler vibrometers using electro-optical modulator. Precis Eng 2025;93:204–15. https://doi.org/10.1016/j.precisioneng.2024.12.015.
[25] Yuan K, Zhu Z, Chen W, Zhu W. Development and validation of a new type of displacement-based miniatured laser vibrometers. Sensors 2024;24:5230. https://doi.org/10.3390/s24165230.
[26] Chatterton S, Dassi L, Gheller E, Ghisi T, Vania A, Pennacchi P. Torsional vibration analysis using rotational laser vibrometers. Sensors 2024;24:1788. https://doi.org/10.3390/s24061788.
[27] Bi C-X, Jing W-Q, Zhang Y-B, Lin W-L. Reconstruction of the sound field above a reflecting plane using the equivalent source method. J Sound Vib 2017;386:149–62. https://doi.org/10.1016/j.jsv.2016.09.029.
[28] Cheng W, Zhang P, Song C, Chen X, Ou K, Han S, et al. A combined sound field reconstruction method for non-cylindrical rotative surfaces based on statistically optimal cylindrical near-field acoustic holography and multipoint helmholtz equation least square. J Vib Control 2023;29:3312–25. https://doi.org/10.1177/10775463221094885.
[29] Zhang F-M, Zhang X-Z, Zhang Y-B, Bi C-X, Zhou R. Sound field reconstruction using sparse bayesian learning equivalent source method with hyperparametric-coupled prior. Appl Acoust 2023;211:109496. https://doi.org/10.1016/j.apacoust.2023.109496.
[30] Geng L, Shen H, He C-D, Chen W, Xie F. Transient sound field reconstruction using time domain nearfield acoustic holography based-variational bayesian augmented kalman filter. Mech Syst Signal Process 2025;229:112540. https://doi.org/10.1016/j.ymssp.2025.112540.
[31] Verburg SA, Fernandez-Grande E, Gerstoft P. Differentiable physics for sound field reconstruction. J Acoust Soc Am 2025;158:4059–69. https://doi.org/10.1121/10.0039862.
[32] Pezzoli M, Carabias-Orti J, Vera-Candeas P, Antonacci F, Sarti A. Spherical-harmonics-based sound field decomposition and multichannel NMF for sound source separation. Appl Acoust 2024;218:109888. https://doi.org/10.1016/j.apacoust.2024.109888.
[33] Qi Q, Chen H, Zhou B, Du J, Yang H. Sound field holographic reconstruction system based on nearfield acoustic holography. In: 2016 IEEE Int. Conf. Signal Process. Commun. Comput. ICSPCC; 2016. p. 1–5. https://doi.org/10.1109/ICSPCC.2016.7753680.
[34] Caviedes-Nozal D, Riis NAB, Heuchel FM, Brunskog J, Gerstoft P, Fernandez-Grande E. Gaussian processes for sound field reconstruction. J Acoust Soc Am 2021;149:1107–19. https://doi.org/10.1121/10.0003497.
[35] Schmid JM, Fernandez-Grande E, Hahmann M, Gurbuz C, Eser M, Marburg S. Spatial reconstruction of the sound field in a room in the modal frequency range using bayesian inference. J Acoust Soc Am 2021;150:4385–94. https://doi.org/10.1121/10.0009040.
[36] Wabnitz A, Epain N, Van Schaik A, Jin C. Time domain reconstruction of spatial sound fields using compressed sensing. In: 2011 IEEE Int. Conf. Acoust. Speech Signal Process. ICASSP; 2011. p. 465–8. https://doi.org/10.1109/ICASSP.2011.5946441.
[37] Verburg SA, Fernandez-Grande E. Reconstruction of the sound field in a room using compressive sensing. J Acoust Soc Am 2018;143:3770–9. https://doi.org/10.1121/1.5042247.
[38] Hu d-Y, Li H-B, Hu Y, Fang Y. Sound field reconstruction with sparse sampling and the equivalent source method. Mech Syst Signal Process 2018;108:317–25. https://doi.org/10.1016/j.ymssp.2018.02.031.
[39] Geng L, Chen X-G, He S-P, He C-D. Reconstruction of transient acoustic field using sparse real-time near-field acoustic holography. J Sound Vib 2024;568:117973. https://doi.org/10.1016/j.jsv.2023.117973.
[40] Wang B, Chen Y, Huang X, An P. A novel EPI-guided network with progressive fusion for light field reconstruction. Expert Syst Appl 2026;296:128964. https://doi.org/10.1016/j.eswa.2025.128964.
[41] Zhai Q, Xu Y, Hu Z, Liu G, Zhao Y, Qu H, et al. OE-diff: observation-embedded diffusion with closed-form guidance and inverse-root scheduling for real-world image super-resolution. Expert Syst Appl 2026;324:132520. https://doi.org/10.1016/j.eswa.2026.132520.
[42] Lai Z, Zhao L, Shao Q. Locally enhanced neural networks for discontinuities in solid mechanics. Int J Mech Sci 2026;322:111660. https://doi.org/10.1016/j.ijmecsci.2026.111660.
[43] Chen L, Chen N, Liu J, Xia B. Spatially adaptable mechanical neural networks with multi fully connected layers. Int J Mech Sci 2026;313:111283. https://doi.org/10.1016/j.ijmecsci.2026.111283.
[44] Chen X-X, Zeng B, Wang X, Sun H, Yin Z-Y. Physics-encoded recurrent graph neural network for long-term consolidation. Int J Mech Sci 2026;314:111414. https://doi.org/10.1016/j.ijmecsci.2026.111414.
[45] Xu K, Zhang N, Yin Z-Y, Li K-Q. Hierarchical physics-guided neural network for sparse-data heterogeneous material identification. Int J Mech Sci 2026;313:111291. https://doi.org/10.1016/j.ijmecsci.2026.111291.
[46] Sun B-X, Liu C-X, Yu G-L, Li J, Liu Z. A novel physics-informed neural network via field mapping. Int J Mech Sci 2026;316:111462. https://doi.org/10.1016/j.ijmecsci.2026.111462.
[47] Huang Y, Yang J, Zhang Y. Wide-range constitutive modeling with multi-fidelity physics-guided neural network. Int J Mech Sci 2026;311:111146. https://doi.org/10.1016/j.ijmecsci.2026.111146.
[48] Zhou X, Song Z, Gao J, Sun Z, Shi S, Guo X. Prediction of sandwich structures combining K-means algorithm with neural network. Int J Mech Sci 2026;316:111468. https://doi.org/10.1016/j.ijmecsci.2026.111468.
[49] Fernandez-Grande E, Karakonstantis X, Caviedes-Nozal D, Gerstoft P. Generative models for sound field reconstruction. J Acoust Soc Am 2023;153:1179–90. https://doi.org/10.1121/10.0016896.
[50] Lluís F, Martínez-Nuevo P, Bo Møller M, Ewan Shepstone S. Sound field reconstruction in rooms: inpainting meets super-resolution. J Acoust Soc Am 2020;148:649–59. https://doi.org/10.1121/10.0001687.
[51] Yang Y, Li H. DualNet: a weight-coupled neural network framework for stable physics-informed learning with order reduction. Expert Syst Appl 2026;327:132832. https://doi.org/10.1016/j.eswa.2026.132832.
[52] Shang L, Zhang Y, Wang J. Local balance for energy-based physics-informed neural networks on phase-field models. Int J Mech Sci 2026;324:111790. https://doi.org/10.1016/j.ijmecsci.2026.111790.
[53] Li S, Nie D, Zhang Y, Li L. Physics-informed neural network-based homogenization for architected lattice structures. Int J Mech Sci 2025;306:110783. https://doi.org/10.1016/j.ijmecsci.2025.110783.
[54] Chen K, Dong X, Gao P, Chen Q, Peng Z, Meng G. Physics-informed neural networks for topological metamaterial design and mechanical applications. Int J Mech Sci 2025;301:110489. https://doi.org/10.1016/j.ijmecsci.2025.110489.
[55] Brecht R, Cardoso-Bihlo E, Bihlo A. Physics-informed neural networks for tsunami inundation modeling. J Comput Phys 2025;536:114066. https://doi.org/10.1016/j.jcp.2025.114066.
[56] Smyl D, Tallman TN, Homa L, Flournoy C, Hamilton SJ, Wertz J. Physics informed neural networks for electrical impedance tomography. Neural Netw 2025;188:107410. https://doi.org/10.1016/j.neunet.2025.107410.
[57] Vasheghani Farahani H, Tahsini AM, Nematollahi A, Ghiasi Afzal M. A novel physics-informed neural network architecture for solving nonlinear PDEs in fluid mechanics without labeled data. Eng Comput 2026;42:46. https://doi.org/10.1007/s00366-026-02277-6.
[58] Ding K, Fu Y, Fang D. A robust constrained-weight physics-informed neural network for forward and inverse analyses of mechanics. Comput Phys Commun 2026;325:110206. https://doi.org/10.1016/j.cpc.2026.110206.
[59] Eivazi H, Wang Y, Vinuesa R. Physics-informed deep-learning applications to experimental fluid mechanics. Meas Sci Technol 2024;35:075303. https://doi.org/10.1088/1361-6501/ad3fd3.
[60] Lai B, Tropea C, Cao J, Liu Y, Lin C, Wen X. Vorticity–velocity physics-informed neural networks for spatio-temporal super-resolution of sub-sampled velocity measurements. J Fluid Mech 2026;1033:A38. https://doi.org/10.1017/jfm.2026.11469.
[61] Zhang Z, Shukla K, Wang Z, Morales A, Käufer T, Salauddin S, et al. Turbulence closure in reynolds-averaged navier–stokes and flow inference around a cylinder using physics-informed neural networks and sparse experimental data. J Fluid Mech 2026;1034:A16. https://doi.org/10.1017/jfm.2026.11471.
[62] Wang C, Ye F, Zhao W, Wang T, Wang S, Wu Y, et al. A dual-branch physics-informed neural network for fluid-structure interaction analysis of aortic valve. J Fluids Struct 2026;146:104643. https://doi.org/10.1016/j.jfluidstructs.2026.104643.
[63] Liu Y, Cai L, Chen Y, Liu Q. Fluid–structure interaction training of integral conservation physics-informed neural networks for blood flow in elastic vessels. Comput Phys Commun 2026;324:110131. https://doi.org/10.1016/j.cpc.2026.110131.
[64] Wang J, Peng Q, Meng J, Liu T, Peng J, Teodorescu R. A physics-informed neural network approach to parameter estimation of lithium-ion battery electrochemical model. J Power Sources 2024;621:235271. https://doi.org/10.1016/j.jpowsour.2024.235271.
[65] Li Z, Li J, Luo Z, Zhang Y, Lin N, Zhang Q. An electrochemical parameter identification method for power batteries based on an improved physics-informed neural network. J Electrochem Soc 2026;173:120513. https://doi.org/10.1149/1945-7111/ae6e21.
[66] Chen L, Chang C, Liu X, Jiang J, Jiang Y, Tian A. Physics-informed neural networks for small sample state of health estimation of lithium-ion batteries. J Energy Storage 2025;122:116559. https://doi.org/10.1016/j.est.2025.116559.
[67] Ahmadi Mousavi ES, Abdollahi F, Barazandeh F, Torabi F, Hajizadeh A. A novel lithium-ion battery remaining useful life prediction method by learning wiener process-based degradation model via physics-informed neural network. Int J Energy Res 2026;2026:9923180. https://doi.org/10.1155/er/9923180.

[68] Gu X, Huan X, Ren Y, Zhou W, Jiang W, Song Z. Real-time physics-aware battery health monitoring from partial charging profiles via physics-informed neural networks. eTransportation 2026;28:100555. https://doi.org/10.1016/j.etran.2026.100555.

[69] Wang F, Zhai Z, Zhao Z, Di Y, Chen X. Physics-informed neural network for lithium-ion battery degradation stable modeling and prognosis. Nat Commun 2024;15:4332. https://doi.org/10.1038/s41467-024-48779-z.

[70] Hu H, Qi L, Chao X. Physics-informed neural networks (PINN) for computational solid mechanics: numerical frameworks and applications. Thin Walled Struct 2024;205:112495. https://doi.org/10.1016/j.tws.2024.112495.

[71] Yin Z, Jiang Y, Guo Y, Pu J, Ma S, Li G-Y, et al. Physics-informed neural networks enable quantitative characterization of viscoelastic properties from shear waves in multiple organs. J Mech Phys Solids 2026;209:106500. https://doi.org/10.1016/j.jmps.2025.106500.

[72] Zhou X, Ma J. Nonlocal energy-encoded physics-informed neural networks for crack propagation in solid materials. J Mech Phys Solids 2026;216:106770. https://doi.org/10.1016/j.jmps.2026.106770.

[73] Chen F, Xiao Y, Yu L, Jiang L. Frequency-domain physics-informed neural network for accurate reconstruction of 3D acoustic fields under sparse and multi-frequency measurements. Neural Netw 2026;197:108476. https://doi.org/10.1016/j.neunet.2025.108476.

[74] Jones LE, Sandham ND, Sandberg RD. Acoustic source identification for transitional airfoil flows using cross correlations. AIAA J. 2010;48:2299–312. https://doi.org/10.2514/1.J050345.

[75] Simard P, Antoni J. Acoustic source identification: experimenting the $\ell 1$ minimization approach. Appl Acoust 2013;74:974–86. https://doi.org/10.1016/j.apacoust.2013.01.012.

[76] Chu Z, Yang Y, Shen L. Resolution and quantification accuracy enhancement of functional delay and sum beamforming for three-dimensional acoustic source identification with solid spherical arrays. Mech Syst Signal Process 2017;88:274–89. https://doi.org/10.1016/j.ymssp.2016.11.027.

[77] Zhao S, Chu Z, Yang Y, Zhang Y. High-resolution CLEAN-SC for acoustic source identification with spherical microphone arrays. J Acoust Soc Am 2019;145:EL598–603. https://doi.org/10.1121/1.5113972.

[78] Zhang X, Chu Z, Yang Y, Zhao S, Yang Y. An alternative hybrid time-frequency domain approach based on fast iterative shrinkage-thresholding algorithm for rotating acoustic source identification. IEEE Access 2019;7:59797–805. https://doi.org/10.1109/ACCESS.2019.2915001.

[79] Sun S, Wang T, Chu F. A generalized minimax-concave penalty based compressive beamforming method for acoustic source identification. J Sound Vib 2021;500:116017. https://doi.org/10.1016/j.jsv.2021.116017.

[80] Sun S, Wang T, Chu F, Tan J. Acoustic source identification using an off-grid and sparsity-based method for sound field reconstruction. Mech Syst Signal Process 2022;170:108869. https://doi.org/10.1016/j.ymssp.2022.108869.

[81] Liao S, Zhu M. General model for acoustic source identification in ducts: one-dimensional model and its verification. J Sound Vib 2026;632:119726. https://doi.org/10.1016/j.jsv.2026.119726.

[82] Yang Y, Yang Y, Chu Z. Off-grid deconvolution beamforming for acoustic source identification. Appl Acoust 2024;218:109909. https://doi.org/10.1016/j.apacoust.2024.109909.

[83] Plaksin GM, Kozubskaya TK, Sofronov IL. On numerical beamforming for acoustic source identification based on supercomputer simulation data. Dokl Math 2024;110:435–41. https://doi.org/10.1134/S1064562424601550.

[84] Li S, Yu Y, Shen P. Two-dimensional off-grid beamforming acoustic source identification for planar microphone arrays via unfolding delay-and-sum. IEEE Sens J 2025;25:20169–84. https://doi.org/10.1109/JSEN.2025.3562960.

[85] Cho J, Nam S, Yang H, Yun S-B, Hong Y, Park E. Separable PINN: mitigating the curse of dimensionality in physics-informed neural networks. Adv Neural Inf Process Syst 2022.

[86] Kang M, Park Y, Song C. How does PDE order affect the convergence of PINNs? Adv Neural Inf Process Syst 2024:73–131. https://doi.org/10.52202/079017-0003.

[87] Wang S, Bhartari AK, Li B, Perdikaris P. Gradient alignment in physics-informed neural networks: a second-order optimization perspective. Adv Neural Inf Process Syst 2025.

[88] Bu D, Byun Y, Lee J-S. Harmonized cone for feasible and non-conflict directions in training physics-informed neural networks. Fourteenth Int Conf Learn Represent 2026.

[89] Zhou C, Li T, Lan C, Du R, Xin G, Li W, et al. Hybrid boundary physics-informed neural networks for solving navier-stokes equations with complex boundary. Adv Neural Inf Process Syst 2025:137350–86.

[90] Sevart CD, Kim J, Shu JI, Wang Y, Simac J, Kaminsky A. Optimal sensor placement for field reconstruction and aerostructural control using state-consistent parametric reduced order models. AIAA scitech 2024 forum. Orlando, FL: American Institute of Aeronautics and Astronautics; 2024. https://doi.org/10.2514/6.2024-2797.

[91] Verburg SA, Elvander F, van Waterschoot T, Fernandez-Grande E. Optimal sensor placement for the spatial reconstruction of sound fields. EURASIP J Audio Speech Music Process 2024;2024:41. https://doi.org/10.1186/s13636-024-00364-4.

[92] Wang Z, Li H-X, Chen C. Reinforcement learning-based optimal sensor placement for spatiotemporal modeling. IEEE Trans Cybern 2020;50:2861–71. https://doi.org/10.1109/TCYB.2019.2901897.

[93] Jabini A, Johnson EA. A deep reinforcement learning approach to sensor placement under uncertainty. IFAC-Pap 2022;55:178–83. https://doi.org/10.1016/j.ifacol.2022.10.508.

[94] Li B, Liu H, Wang R. Data-driven sensor placement for efficient thermal field reconstruction. Sci China Technol Sci 2021;64:1981–94. https://doi.org/10.1007/s11431-020-1829-2.

[95] Farid M, Solav D. Data-driven sensor placement optimization for accurate and early prediction of stochastic complex systems. J Sound Vib 2023;543:117317. https://doi.org/10.1016/j.jsv.2022.117317.

[96] Manohar K, Brunton BW, Kutz JN, Brunton SL. Data-driven sparse sensor placement for reconstruction. IEEE Control Syst 2018;38:63–86. https://doi.org/10.1109/MCS.2018.2810460.

[97] Meng X, Zhang H, Jia K, Li H, Huang Y. Optimal sensor placement for structural health monitoring based on deep reinforcement learning. Smart Struct Syst 2023;31:247–57. https://doi.org/10.12989/SSS.2023.31.3.247.

[98] Li B, Zhao Y-P, Wu H, Tan H-J. Optimal sensor placement using data-driven sparse learning method with application to pattern classification of hypersonic inlet. Mech Syst Signal Process 2021;147:107110. https://doi.org/10.1016/j.ymssp.2020.107110.

[99] Cao J, Bu F, Wang J, Bao C, Chen W, Dai K. Reconstruction of full-field dynamic responses for large-scale structures using optimal sensor placement. J Sound Vib 2023;554:117693. https://doi.org/10.1016/j.jsv.2023.117693.

[100] Paris R, Beneddine S, Dandois J. Robust flow control and optimal sensor placement using deep reinforcement learning. J Fluid Mech 2021;913:A25. https://doi.org/10.1017/jfm.2020.1170.

[101] Marcato A, Guiltinan E, Viswanathan H, O'Malley D, Lubbers N, Santos JE. Journey over destination: dynamic sensor placement enhances generalization. Mach Learn Sci Technol 2024;5:025070. https://doi.org/10.1088/2632-2153/ad4e06.

[102] Liu X, Peng W, Zhang X, Zhao X, Zhou W, Yao W, et al. Enhancing deep learning-based field reconstruction with a differentiable learning framework. Nat Mach Intell 2025;7:1129–40. https://doi.org/10.1038/s42256-025-01063-1.

[103] Duraiswami R, Gumerov N. The wave and helmholtz equations. U Md 2006.

[104] Sklyanin EK. Separation of variables: new trends. Prog Theor Phys Suppl 1995;118:35–60. https://doi.org/10.1143/PTPS.118.35.

[105] Liu Q, Chu M, Thuerey N. ConFIG: towards conflict-free training of physics informed neural networks. Int Conf Learn Represent 2024;2025:59531–66.

[106] Liu L, Li Y, Kuang Z, Xue J-H, Chen Y, Yang W, et al. Towards impartial multi-task learning. In: Int. Conf. Learn. Represent; 2021.

[107] Yu T, Kumar S, Gupta A, Levine S, Hausman K, Finn C. Gradient surgery for multi-task learning. Adv Neural Inf Process Syst 2020;33:5824–36.